



Cite this: *EES Catal.*, 2026, 4, 118

Phosphate modification of Pd/Al₂O₃ enhances activity and stability in aromatic hydrogenation under CO-contaminated hydrogen

Adrian Seitz,^a Yaoci Sheng,^b Ian Backes,^a Phillip Nathrath,^a Dennis Weber,^{ac} Tanja Franken,^{ib ac} Roberto Félix,^{id} Angelo Rillera,^d Johannes Frisch,^{de} Marcus Bär,^{ib defg} Tanja Retzer,^{ib} and Patrick Schühle^{ib *a}

Hydrogenation reactions are essential to synthesize platform and fine chemicals today and to establish chemical hydrogen storage in the future. However, hydrogen from fossil or biogenic sources contains CO, a potent poison for noble metal hydrogenation catalysts, necessitating costly purification steps. In this work, we demonstrate phosphate modification as an effective strategy to enhance activity and CO tolerance of Pd/Al₂O₃ in benzyltoluene hydrogenation using pure and impure H₂ streams. Under 1.6 vol% CO in H₂, phosphate modified catalysts achieve a 230% increase in productivity over unmodified Pd/Al₂O₃. Characterization reveals that highly dispersed monomeric phosphate species on Al₂O₃ enhance metal–support interaction and induce Pd redispersion, forming smaller, more stable Pd nanoparticles with enhanced resistance against sintering. Notably, the local electronic environment of Pd remains unchanged by phosphate species. We further show that under CO-rich conditions, benzyltoluene is preferentially hydrogenated at Pd edge sites rather than terrace sites, which explains the pronounced activity increase of the smaller Pd nanoparticles. Phosphate-induced acidity provides additional sites for aromatic hydrogenation with spilled-over hydrogen that remain active in the presence of CO.

Received 29th July 2025,
 Accepted 26th September 2025

DOI: 10.1039/d5ey00231a

rsc.li/eescatalysis

Broader context

Catalytic hydrogenation is one of the most important reactions in the chemical industry, essential for the production of a wide range of bulk and fine chemicals, as well as pharmaceuticals. However, many hydrogenation processes require high-purity hydrogen, as conventional catalysts are highly susceptible to trace impurities such as carbon monoxide (CO). Removing these impurities involves costly and energy-intensive purification steps, which increase both operational complexity and environmental impact. In this work, we present phosphate modification as a strategy to enhance the CO tolerance of Pd/Al₂O₃ catalysts while simultaneously enhancing their activity and thermal stability. This allows the use of impure hydrogen from renewable or circular sources such as biomass or plastic waste, significantly reducing energy demand for purification. Beyond conventional hydrogenation, the findings are also highly relevant for hydrogen storage technologies based on liquid organic hydrogen carriers (LOHCs), where hydrogenation with impure hydrogen enables the integration of purification and storage into a single process step.

^a Institute of Chemical Reaction Engineering, Friedrich-Alexander-Universität Erlangen-Nürnberg, Egerlandstraße 3, 91058 Erlangen, Germany.
 E-mail: patrick.schuehle@fau.de

^b Interface Research and Catalysis, ECRC, Friedrich-Alexander-Universität Erlangen-Nürnberg, Egerlandstraße 3, 91058 Erlangen, Germany

^c Technical Chemistry I, Technische Universität Darmstadt, Peter-Grünberg-Straße 8, 64287 Darmstadt, Germany

^d Department Interface Design, Helmholtz-Zentrum Berlin für Materialien und Energie GmbH (HZB), Albert-Einstein-Straße 15, 12489 Berlin, Germany

^e Energy Materials In Situ Laboratory Berlin (EMIL), Helmholtz-Zentrum Berlin für Materialien und Energie GmbH (HZB), Albert-Einstein-Straße 15, 12489 Berlin, Germany

^f Lehrstuhl für Physikalische Chemie II, Friedrich-Alexander-Universität Erlangen-Nürnberg, Egerlandstraße 3, 91058 Erlangen, Germany

^g Department for X-ray Spectroscopy at Interfaces of Thin Films, Helmholtz-Institute Erlangen-Nürnberg for Renewable Energy, Albert-Einstein-Str. 15, 12489 Berlin, Germany

Introduction

Hydrogenation of unsaturated hydrocarbons is a fundamental reaction employed in numerous synthesis steps across the chemical industry, including the production of bulk and fine chemicals, pharmaceuticals, and agrochemicals.^{1,2} Currently, hydrogen used in hydrogenation processes is predominantly produced *via* steam reforming and gasification of fossil-based resources. In the future, water electrolysis is expected to dominate hydrogen production; however, sustainable feedstock such as biomass residues and plastic waste can be converted to hydrogen, offering pathways to decarbonize traditional technologies like gasification and steam reforming today.



Regardless of the feedstock, these processes yield impure hydrogen, typically contaminated with CO_2 , CH_4 , and CO . To obtain hydrogen in high purity, as required for sensitive chemical and catalytic transformations, extensive purification processes are necessary, including reactive steps (e.g., water-gas shift reaction, CO_x methanation) and thermal methods (e.g., adsorption, absorption). Prior to hydrogenation of hydrocarbons, hydrogen purification is critical because noble metal catalysts applied therein are highly susceptible to poisoning by impurities, particularly CO .^{3,4} Developing hydrogenation catalysts that remain stable in the presence of such contaminants, thus eliminating the need for extensive purification, has the potential to significantly enhance process profitability, as demonstrated in a techno-economic assessment.⁵

In the context of a future hydrogen economy, hydrogenation reactions are expected to gain even greater importance.⁶ Liquid organic hydrogen carrier (LOHC) systems enable the storage of hydrogen in liquid form, allowing for its transport and storage using existing liquid fuel infrastructure.^{7,8} In these systems, sustainably produced hydrogen is used to catalytically hydrogenate an H_2 -lean LOHC molecule, such as benzyltoluene (H0-BT). At the location and time of hydrogen demand, dehydrogenation of the H_2 -rich LOHC molecule, such as perhydrobenzyltoluene (H12-BT), releases high-purity H_2 . While the LOHC technology has primarily been developed to store green hydrogen from water electrolysis, it can also be applied to hydrogen produced from alternative sustainable resources, such as biomass or plastic waste. In this context, directly utilizing impure H_2 for LOHC hydrogenation integrates purification and chemical storage into a single process step, significantly simplifying the overall process. As illustrated in Fig. 1, H0-BT is selectively hydrogenated using hydrogen contaminated with impurities.^{3,8} Unlike H_2 , the impurities CO_2 , CH_4 and CO do not react with the LOHC molecule and remain in the gas phase, allowing for their separation. Upon dehydrogenation of H12-BT, high-purity H_2 is subsequently released from the LOHC molecule, using well-known dehydrogenation catalysts.^{9,10}

Few studies have investigated suitable catalysts for the hydrogenation of aromatic rings using impure H_2 . A screening of active metals (Co, Ni, Ru, Rh, Pd and Pt) supported on Al_2O_3 for naphthalene hydrogenation in the presence of 2% CO revealed no activity for Pt, Ru and Rh.⁴ Co and Ni exhibited moderate naphthalene hydrogenation activities; however, these catalysts also promoted CO methanation.⁴ Similar behavior was observed for $\text{Ni}/\text{SiO}_2\text{-Al}_2\text{O}_3$ ¹¹ and RuNi/TiO_2 ¹² catalysts, the latter showing stable operation for up to 25 hours. It is important to note that CO_x methanation consumes valuable hydrogen, reducing its availability for aromatic hydrogenation.

The same study demonstrated, that $\text{Pd}/\text{Al}_2\text{O}_3$ combines the highest activity in aromatic hydrogenation with the lowest activity in CO methanation.⁴ In agreement, $\text{Pd}/\text{Al}_2\text{O}_3$ was identified as an effective and stable catalyst for the hydrogenation of the LOHC molecule dibenzyltoluene in the presence of CH_4 (up to 50% gas content),¹³ CO_2 (up to 30%)¹⁴ and CO (up to 10%)¹⁵ in a semi-continuous reactor. While CH_4 was found to remain mostly inert,¹³ CO contamination significantly reduced hydrogenation activity compared to the benchmark using pure hydrogen.¹⁵ CO_2 posed additional challenges due to its conversion to CO via the reverse water-gas shift (RWGS) reaction.^{14,16,17} Consequently, to increase hydrogenation activity with impure hydrogen, the impurity tolerance of $\text{Pd}/\text{Al}_2\text{O}_3$ must be further improved. One strategy to modify catalytic characteristics is doping with main group elements, such as phosphorus,^{18–25} which could enable the fine-tuning of relevant bond strengths, e.g., of reactants, products, and rate-inhibiting spectator molecules such as CO .

For instance, phosphorus doping of $\text{Pt}/\text{Al}_2\text{O}_3$ significantly enhanced propylene selectivity in propane dehydrogenation.²³ This improvement was attributed, among other factors, to altered reactant adsorption properties.²³ For example, CO adsorption studies revealed a suppression of strongly adsorbed CO species in bridge and three-fold hollow configurations on modified catalysts.²³ These findings suggest that phosphorus modification could be highly beneficial for hydrogenation reactions, particularly in the presence of impurities like CO .

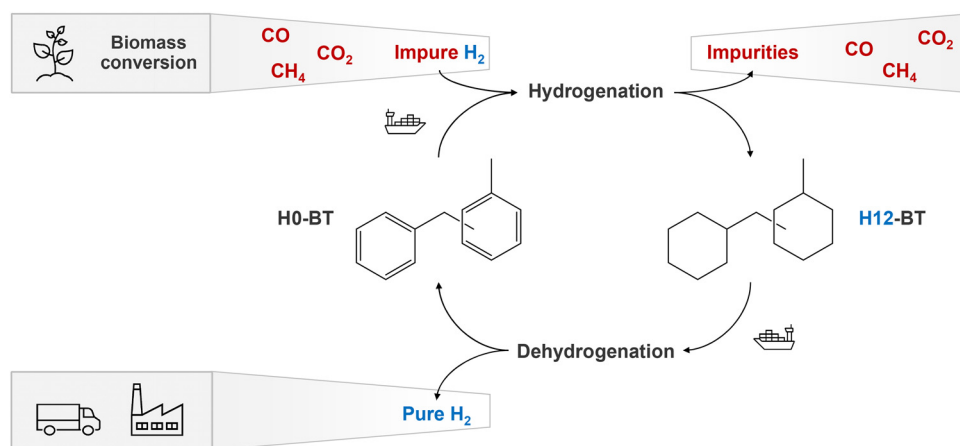


Fig. 1 LOHC hydrogenation with impure hydrogen from biogenic sources allows for chemical hydrogen storage and purification in a single process step.



Phosphorus doping of Pt/Al₂O₃ was further shown to result in the formation of phosphate (PO_x) species, due to the strong interaction between P and Al₂O₃.^{23–25} These PO_x species were proposed by some of us to act as an anchor at the metal–support interface.²⁴ It was demonstrated that these PO_x species induce exceptional stability against sintering, conserving Pt particles smaller than 2 nm at temperatures up to 900 °C.²⁴ Such Pt-PO_x/Al₂O₃ catalysts were already studied in the context of LOHC-based hydrogen storage. Particularly, they exhibited higher activity in the dehydrogenation of H12-BT compared to unmodified Pt/Al₂O₃.^{24,25}

In this contribution, we study PO_x modification as a strategy to increase the activity of Pd/Al₂O₃ catalysts in hydrogenation of the aromatic LOHC compound H0-BT. We demonstrate that the concept of PO_x modification, previously described as beneficial for Pt/Al₂O₃, is transferable to Pd/Al₂O₃ and thus potentially generalizable. In addition to increasing activity and stability towards sintering, we investigate whether PO_x modification can also increase the CO poisoning tolerance of Pd catalysts. This would open up a way to significantly reduce the purification effort for hydrogen streams and thus make hydrogen technologies more cost-efficient.

Experimental

Catalyst preparation

A commercial Pd/Al₂O₃ powder catalyst containing 4 wt% Pd was purchased (Merck KGaA). Four different lots of the same product (lot 1: MKCQ6812, lot 2: MKCR3779, lot 3: MKCT2316, lot 4: MKBH9857) were utilized for catalytic studies and characterization. Unless stated otherwise, the catalyst was employed as received without further modification and is referred to as Pd/Al₂O₃. Thermal treatments of Pd/Al₂O₃ were carried out in a tubular furnace by heating to the target temperature (400–700 °C, 10 K min⁻¹) under a N₂ atmosphere. The target temperature was maintained for two hours under either pure N₂ or a 10% H₂/N₂ mixture (total flow: 500 mL min⁻¹). These catalysts are referred to according to their treatment temperature, e.g., the sample that has been thermally treated in the above described way to a target temperature of 400 °C is referred to as Pd-400/Al₂O₃. The Pd-PO_x/Al₂O₃ catalysts were synthesized *via* wet impregnation of Pd/Al₂O₃ with an aqueous solution of H₃PO₃. The mixture was stirred for 16 h, followed by solvent removal at 80 °C under reduced pressure (100 mbar). Subsequent thermal treatments were performed as described above. Catalysts were designated based on the molar P : Pd ratio and the thermal treatment temperature; for example, a catalyst with a ratio of 1.7 and a thermal treatment temperature of 600 °C is referred to as Pd-PO_x-1.7-600/Al₂O₃.

Benzyltoluene hydrogenation experiments with pure H₂

Hydrogenation experiments were conducted in a 300 mL batch autoclave (Parr type 4566) with a four-blade gas-inducing stirrer, an electric heating mantle, a cooling coil connected to a cryostat (Huber Unichiller 022), a thermocouple (type J), a

pressure recorder (Ashcroft type G2), a process controller (Parr type 4875) and a liquid sampling line fitted with a filter and needle valve. The reactor was initially charged with 0.55 mol H0-BT (Eastman Chemical Company) and a specific amount of Pd/Al₂O₃ or Pd-PO_x/Al₂O₃. The catalyst mass was adjusted to reach an $n_{\text{Pd}} : n_{\text{H0-BT}}$ molar ratio of 4.1×10^{-4} . After sealing the reactor with a Kalrez[®] 4079 O-ring, it was purged four times with argon (3 bar_g). The reactor was then heated to a target temperature between 230–250 °C, while stirring at 300 min⁻¹. Upon reaching the desired temperature, the liquid sample line was flushed with 1 mL of reaction liquid, and 0.1 mL was collected for gas chromatography (GC) analysis. Additional samples were taken at various intervals during the reaction. The reaction was initiated by adding 30 bar of H₂ and increasing the stirrer speed to 1200 min⁻¹ ($t = 0$ min). Experiments were conducted in dead-end mode, maintaining constant H₂ pressure by continuously supplying H₂ to compensate for its consumption during the reaction.

Benzyltoluene hydrogenation experiments with impure H₂

Hydrogenation experiments with impure H₂ were prepared as described above. After reaching the target temperature, the reactor was charged with a synthetic gas mixture (Linde) containing H₂ and impurities (CO, CO₂ and/or CH₄). This way the reactor was charged to the desired impurity partial pressures. Subsequently, the H₂ pressure was adjusted to 30 bar by adding pure H₂. After increasing the stirrer speed to 1200 min⁻¹, pressure drop due to hydrogenation was compensated by continuously feeding pure H₂, maintaining constant pressure throughout the experiment. For experiments with only CO as impurity (H₂/CO), a CO concentration of 1.6 vol% was used. For experiments with mixed CO₂, CH₄ and CO impurities (H₂/mixed), cumulative impurity concentrations of 12, 22 and 36 vol% were achieved, maintaining a fixed volumetric impurity ratio of 32:3:1 (CO₂:CH₄:CO), corresponding to typical impurity concentrations of a H₂-rich mixed gas after a water-gas shift step.^{8,26} The corresponding impurity partial pressures and concentrations for H₂/CO and H₂/mixed experiments are summarized in Table S1. The $n_{\text{Pd}} : n_{\text{H0-BT}}$ ratio in the reactor was adjusted to 5.1×10^{-4} for H₂/CO and 4.1×10^{-4} for H₂/mixed experiments.

Calculation of performance indicators

30 μL of each liquid product sample was dissolved in 1 mL acetone (≥99.8% Merck KGaA) and analyzed in a Shimadzu GC-2010 Plus equipped with a flame ionization detector (FID) and a Restek Rxi-17Sil column. Qualitative and quantitative calibration of H0-, H6- and H12-BT peaks is described elsewhere.²⁷ H6-BT corresponds to a benzyltoluene molecule with one of the two aromatic rings hydrogenated. The degree of hydrogenation (DoH) of the LOHC system is calculated from the peak areas A_i of H0-, H6- and H12-BT.

$$\text{DoH} = \frac{A_{\text{H12-BT}} + 0.5A_{\text{H6-BT}}}{A_{\text{H12-BT}} + A_{\text{H6-BT}} + A_{\text{H0-BT}}} \times 100\%$$

The productivity $P_{x-y\%}$ gives the mass of H₂ that is reversibly



stored in the LOHC system per mass of Pd and reaction time in a certain DoH range. For experiments with pure H₂, the productivity $P_{10-30\%}$ was calculated within a DoH range of 10–30%, corresponding to reaction times $t_{10\%}$ and $t_{30\%}$. For experiments with gaseous impurities, the initial productivity $P_{1-15\%}$ was determined at reaction times before significant conversion of the impurities could take place. The stoichiometric factor of hydrogen ν_{H_2} corresponds to 6 mol of H₂ that can be bound per mole of H0-BT. The mass of palladium in the reactor m_{Pd} was determined *via* the added catalyst mass and the Pd-loading determined from ICP-OES.

$$P_{x-y\%} = \frac{n_{\text{H0-BT}} \nu_{\text{H}_2} M_{\text{H}_2} (y\% - x\%)}{m_{\text{Pd}} (t_{y\%} - t_{x\%})}$$

The relative productivity change $\Delta P_{x-y\%}$ due to PO_x modification (when compared to unmodified Pd/Al₂O₃) is calculated from $P_{x-y\%}$ of Pd-PO_x/Al₂O₃ and Pd/Al₂O₃ at identical reaction conditions, respectively.

$$\Delta P_{x-y\%} = \left(\frac{P_{x-y\%, \text{Pd-PO}_x} - P_{x-y\%, \text{Pd}}}{P_{x-y\%, \text{Pd}}} \right) \times 100\%$$

Catalyst characterization

Temperature-programmed CO₂ hydrogenation. To investigate the side reactions during H0-BT hydrogenation with impure hydrogen (CO₂ methanation, RWGS reaction and CO methanation) without the presence of H0-BT, continuous gas-phase CO₂ hydrogenation experiments were conducted with the synthesized Pd-catalysts. This was done in a fixed-bed reactor with an internal diameter of 10 mm, equipped with mass flow controllers (Bronkhorst) and a Pfeiffer Vacuum OmniStar GSD 350 mass spectrometer. For each experiment, 500 mg of catalyst was mixed with 2.5 g of quartz sand. Prior to reaction, catalysts underwent *in situ* pre-treatment at 400 °C for 1 hour under a flow of 10% H₂/Ar. The reaction was carried out at ambient pressure using a H₂:CO₂:Ar ratio of 4:1:11 at a total flow rate of 52.4 mL min⁻¹, corresponding to a gas hourly space velocity (GHSV) of 2000 h⁻¹.

Inductively coupled plasma optical emission spectroscopy (ICP-OES). Pd- and P-loadings of the catalysts were measured by digesting 100 mg of catalyst sample in a 10 mL solution of HNO₃/HCl with a volumetric ratio of 4:6 during microwave heating at 200 °C. After digestion, the solution was diluted to 100 mL with deionized water and analyzed using a Ciroc CCD from SPECTRO Analytical Instruments GmbH.

N₂ physisorption. N₂ physisorption was performed at -196 °C in a Quadrasorb SI by Quantachrome Instruments after outgassing the fresh catalyst for 12 hours at 250 °C under vacuum. The specific surface area was calculated by using the Brunauer–Emmett–Teller (BET) method in a p/p_0 range of 0.05–0.35. The total pore volume was determined at $p/p_0 = 0.99$. The average pore diameter was calculated assuming cylindrical pores.

CO-pulse chemisorption. CO-pulse experiments were conducted using an Autochem II 2920 by Micromeritics equipped with a TCD detector and 50 mg of sample. *In situ* pre-treatment

was performed by heating up under Ar to 200 °C at 10 K min⁻¹ and 30 min holding time. After cooling back to room temperature, *in situ* reduction was performed by heating up under 10% H₂/Ar from 40 °C to 200 °C at 5 K min⁻¹. Finally, CO-pulse was conducted at 40 °C with 10% CO/He. The Pd dispersion was calculated by the difference of pulsed and measured CO volume, assuming ideal gas and a stoichiometric CO: Pd factor of 1.

X-ray diffraction (XRD). XRD patterns were obtained using a Pananalytical X-Pert Pro-MD (Philips) equipped with a Cu-K_α radiation source ($\lambda = 0.154$ nm). Measurements were conducted with a scan speed of 0.02° s⁻¹ in an angular range of 10–90°.

High-resolution transmission electron microscopy (HR-TEM). HR-TEM images were acquired using a Philips CM30. Particle diameters were analyzed with the software ImageJ.²⁸ The number of analyzed particles per catalyst N_p was 160–230, yielding an average particle diameter $d_{p,av}$ with a standard deviation SD. The dispersion D was calculated using the Sauter mean diameter, the volume occupied by a Pd atom in the bulk (14.70 Å³) and the surface area occupied by a Pd atom on a polycrystalline surface (7.93 Å²).²⁹

X-ray absorption spectroscopy (XAS). Pd L₃-edge and P K-edge X-ray absorption near edge structure (XANES) spectroscopy and Pd L₂-edge extended X-ray absorption fine structure (EXAFS) spectroscopy were conducted using the high kinetic energy electron (HiKE) end-station³⁰ located at the KMC-1 beamline³¹ of BESSY II, operated by HZB. Since the Pd L₃-edge is interrupted by the onset of the Pd L₂-edge after ~160 eV, EXAFS measurements were performed at the Pd L₂-edge. Monochromatization of the incoming X-rays was achieved using a Si(111) double-crystal monochromator. Spectra were acquired in partial fluorescence yield (PFY) mode, with a Bruker XFlash 4010 silicon drift detector (SDD). Photon energy calibration was conducted by hard X-ray photoelectron spectroscopy (HAXPES) measurements of a clean Au foil. The low and high energy limits of the selected XAS energy ranges were used as excitation energy during calibration and the binding energy of the Au 4f_{7/2} core level was assumed to be 84.0 eV. Prior to XAS normalization, a linear background was fitted and subtracted from each spectrum. XAS normalization and EXAFS analysis was conducted using Larch.³² XANES edge positions are based on the maximum of the 1st derivative of the normalized XANES spectra. First shell EXAFS fitting was performed in an R -range from 1.3 to 3.8 Å. The amplitude reduction factor (S_0^2) was determined from fitting PdO and subsequently fixed at 0.89. During fitting, the energy shift (ΔE_0), coordination numbers (CN), interatomic distances (r) and the Debye–Waller factor (σ^2), which reflects the mean square deviation of interatomic distances, were treated as variables. The R -factor is reported as a measure of fit quality. The measured reference compounds Pd foil, PdO, H₃PO₃, H₃PO₄ and AlPO₄ were purchased from Merck KGaA. The reference compound Pd₃P/SiO₂ was self-synthesized, with the synthesis procedure described in the supporting information. The corresponding XRD pattern of this sample is shown in Fig. S1. Catalyst samples were *ex situ* pre-reduced for 2 h at 400 °C and transported under an Ar atmosphere to HiKE.



Temperature-programmed desorption (TPD) of NH₃/CO. TPD experiments were conducted using an Autochem II 2920 by Micromeritics equipped with a thermal conductivity detector (TCD) and 50 mg (CO-TPD) or 100 mg (NH₃-TPD) of sample. *In situ* pre-treatment was performed by heating up under Ar to 200 °C at 10 K min⁻¹ and 30 min holding time. Further, the sample was heated up under 10% H₂/Ar from 40 °C to 600 °C at 5 K min⁻¹. After cooling back to room temperature, the samples were saturated with CO at 50 °C or NH₃ at 100 °C and subsequently purged at the same temperature with He to remove physisorbed molecules. The sample was then cooled to the TPD starting temperature of 40 °C and heated up to 600 °C at 15 K min⁻¹.

Diffuse reflectance infrared Fourier transform spectroscopy (CO-DRIFTS). *In situ* DRIFTS measurements were performed with a Vertex 80v Fourier transform infrared (FTIR) spectrometer (Bruker) equipped with a KBr beam splitter, a N₂-cooled HgCdTe-detector, and a Praying Mantis DRIFTS accessory with a high temperature reaction chamber located in the home-built extension of the sample compartment of the spectrometer. The complete beam path remains evacuated during the measurements, which leads to excellent long-term stability of the system. The reactor contains a sample cell for powders and is equipped with CaF₂ windows and connections for gas dosing. A thermocouple (type K) has direct contact with the sample powder to monitor the temperature. Ar (Linde, >99.999%) and CO (Linde, >99.997%) gas flows are regulated by mass flow and pressure controllers (Bronkhorst). We performed DRIFTS measurements with an identical gas dosing sequence to all samples and γ -Al₂O₃ as reference material. We purged with Ar to remove residual moisture and air after loading the sample powder into the sample holder and assembly of the reactor. The background spectrum (scan time: 10 min) was recorded in Ar atmosphere. For the temperature-programmed CO-DRIFTS experiments, we filled the reactor with 1 bar CO at a flow rate of 8 mL_N min⁻¹ and maintained a total pressure of 1 bar during the whole measurement. After the recorded spectra were stable, a heating program was initiated to stepwise increase the temperature from 30 °C to 240 °C (heating rate of 5 K min⁻¹). Note that 240 °C represents the reaction temperature during our hydrogenation experiments. This temperature was maintained for 1 h before the system was cooled down to room temperature at the same rate. A schematic representation of the experiments is given in Fig. S2. DRIFT spectra were recorded with a resolution of 2 cm⁻¹ throughout the process (scan time: 0.9 min). Post-data treatment including normalization, baseline correction, and mathematical removal of the CO gas phase were described elsewhere.³³

Results

Benzyltoluene hydrogenation with pure H₂

To investigate the effect of PO_x modification on the hydrogenation of benzyltoluene using pure H₂, we tested Pd-PO_x-600/Al₂O₃ catalysts with varying $n_p:n_{Pd}$ ratios as shown in Fig. 2a.

For this series, all PO_x-modified catalysts were thermally treated under an H₂ atmosphere at 600 °C in an external tubular oven, a procedure previously identified as optimal for Pt-PO_x/Al₂O₃.²⁴ In the hydrogenation reaction all tested $n_p:n_{Pd}$ ratios between 0.5 and 3.0 lead to a productivity increase compared to pristine Pd/Al₂O₃, while ratios exceeding 4.5 lead to a lower productivity. We observe a volcano-type relationship between productivity and $n_p:n_{Pd}$ ratio, with Pd-PO_x-1.9-600/Al₂O₃ reaching maximum productivity (2.70 g_{H₂} g_{Pd}⁻¹ min⁻¹) and a 61% relative improvement compared to Pd/Al₂O₃. Note that the same modification was not effective for Pd/SiO₂ or Pd/C and instead led to lower productivities compared to the respective unmodified samples (Fig. S3). Following this series, a new lot (lot 2) of the commercial Pd/Al₂O₃ catalyst was used. A shortened study with varying $n_p:n_{Pd}$ ratios was conducted with this new lot (Fig. S4), reaching similar results. Since $n_p:n_{Pd}$ ratios between 1.4 and 2.0 (1.7 ± 0.3) yielded the best results for both catalyst lots, samples within this optimal range are collectively referred to as Pd-PO_x-1.7/Al₂O₃.

Next, we investigated the effect of thermal treatment conditions on productivity while maintaining a constant $n_p:n_{Pd}$ ratio (1.7 ± 0.3), as shown in Fig. 2b. For pristine Pd/Al₂O₃, thermal treatment under H₂ at 600 °C results in a productivity decrease from 2.11 to 1.80 g_{H₂} g_{Pd}⁻¹ min⁻¹. In contrast, all PO_x-modified catalysts thermally treated between 500 °C and 700 °C under H₂ exhibit increased productivity compared to Pd/Al₂O₃. Thermal treatment at 600 °C under H₂ yields the highest productivity of 3.08 g_{H₂} g_{Pd}⁻¹ min⁻¹. Notably, replacing H₂ with inert N₂ during the thermal treatment at 600 °C results in a similar productivity enhancement. Based on these findings, all subsequent experiments were conducted using Pd-PO_x-600/Al₂O₃ with thermal treatment under H₂ atmosphere.

The reaction temperature was varied between 230 °C and 250 °C for both Pd/Al₂O₃ and Pd-PO_x-1.7-600/Al₂O₃, and Arrhenius plots were generated (Fig. S5). The obtained apparent activation energies are 63.8 kJ mol⁻¹ (Pd/Al₂O₃) and 68.5 kJ mol⁻¹ (Pd-PO_x-1.7-600/Al₂O₃), showing similar values for both catalysts.

Benzyltoluene hydrogenation with impure H₂

To evaluate the impact of PO_x modification on catalyst resistance against poisoning by impurities during hydrogenation, we tested Pd-PO_x-600/Al₂O₃ with varying $n_p:n_{Pd}$ ratios using a 1.6 vol% CO/H₂ gas mixture (Fig. 3a). The productivity of Pd/Al₂O₃ under these conditions is 0.21 g_{H₂} g_{Pd}⁻¹ min⁻¹, retaining only ~10% of its productivity compared to experiments with pure H₂. In contrast, Pd-PO_x-600/Al₂O₃ with $n_p:n_{Pd}$ ratios in the range of 1.4–2.9 exhibits significantly higher productivities under H₂/CO mixture, with a broad optimum observed for $n_p:n_{Pd}$ ratios between 1.4 and 2.3. The highest productivity reached was 0.65 g_{H₂} g_{Pd}⁻¹ min⁻¹, corresponding to ~20% of the productivity observed with pure H₂. This represents a 233% increase compared to Pd/Al₂O₃ under the same conditions with the H₂/CO mixture, a relative value that is still much lower (61%) in the experiments with pure H₂. The relative productivity difference between PO_x-modified catalysts and the



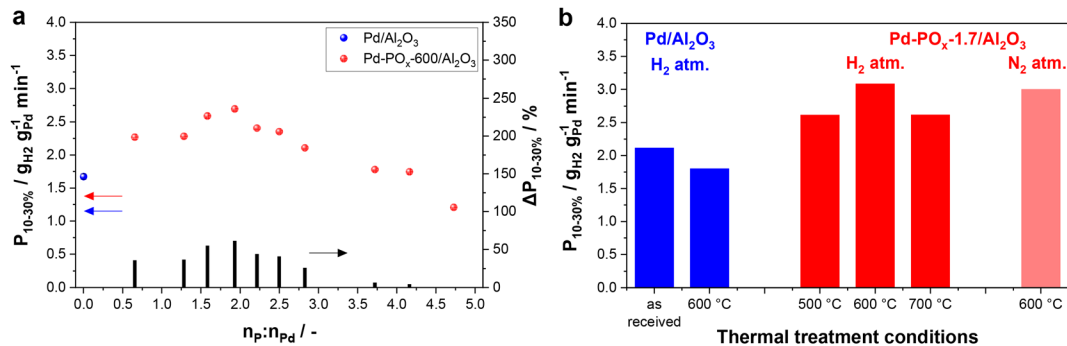


Fig. 2 H0-BT hydrogenation with pure H_2 at 240 °C, 30 bar H_2 -pressure and $n_{\text{Pd}} : n_{\text{H}_0\text{-BT}} = 4.1 \times 10^{-4}$. (a) $P_{10-30\%}$ of $\text{Pd}/\text{Al}_2\text{O}_3$ and $\text{Pd-PO}_x\text{-600}/\text{Al}_2\text{O}_3$ at different $n_P : n_{\text{Pd}}$ ratios (lot 1). (b) $P_{10-30\%}$ of $\text{Pd}/\text{Al}_2\text{O}_3$ and $\text{Pd-PO}_x\text{-1.7}/\text{Al}_2\text{O}_3$ ($n_P : n_{\text{Pd}} = 1.7 \pm 0.3$) prepared under different treatment conditions (lot 2).

benchmark, $\Delta P_{x-y\%}$, is used as a measure to evaluate the extent of enhanced tolerance to impurity poisoning. Moreover, comparison with existing studies on aromatic hydrogenation in H_2/CO mixtures shows that, to the best of our knowledge, $\text{Pd-PO}_x/\text{Al}_2\text{O}_3$ achieves the highest reported productivity when normalized to the mass of active metal (Fig. S6 and Table S2).

Fig. 3b shows the Arrhenius plots for $\text{Pd}/\text{Al}_2\text{O}_3$ and $\text{Pd-PO}_x\text{-1.7-600}/\text{Al}_2\text{O}_3$ under H_2/CO conditions in the temperature range of 220 °C to 250 °C. For $\text{Pd}/\text{Al}_2\text{O}_3$, the addition of CO results in a distinct increase in the apparent activation energy from 63.8 to 155.6 kJ mol^{-1} . Notably, the PO_x -modified catalyst shows a significantly lower apparent activation energy under H_2/CO conditions of 124.7 kJ mol^{-1} , corresponding to a reduction of $\sim 30 \text{ kJ mol}^{-1}$.

Apart from the most critical impurity CO, real gas mixtures from biomass or plastic conversion contain CO_2 and CH_4 impurities. Therefore, we tested $\text{Pd-PO}_x\text{-1.7-600}/\text{Al}_2\text{O}_3$ under an H_2 gas mixture containing CO_2 , CH_4 and CO in a volumetric ratio of 32:3:1. Fig. 4 shows the productivity of $\text{Pd}/\text{Al}_2\text{O}_3$ and $\text{Pd-PO}_x\text{-1.7-600}/\text{Al}_2\text{O}_3$ at varying cumulative impurity concentrations between 0 and 36 vol%. Detailed concentrations and partial pressures of each impurity are provided in Table S1. With increasing cumulative impurity concentration, a steady decline in productivity is observed for both catalysts, in line with previous studies of $\text{Pd}/\text{Al}_2\text{O}_3$.¹⁵ However, $\text{Pd-PO}_x\text{-1.7-600}/\text{Al}_2\text{O}_3$ consistently outperforms $\text{Pd}/\text{Al}_2\text{O}_3$ across all gas

mixtures. $\Delta P_{x-y\%}$ increases from 46% to 135% as the impurity concentration is increased. Interestingly, at the highest impurity concentration of 36 vol%, this trend does not persist, with $\Delta P_{1-15\%}$ dropping below 100%. It is worth noting that these relative values are generally lower than $\Delta P_{1-15\%}$ under H_2/CO conditions (233%).

To evaluate the potential negative effect of CO_2 or CH_4 on the hydrogenation activity, experiments with a cumulative impurity concentration of 36 vol% are directly compared to those conducted with the H_2/CO mixture (Fig. S7). In both cases, the H_2 partial pressure (30 bar) and CO partial pressure (0.5 bar) are identical (see Table S1). In the H_2/mixed experiments, additional CO_2 (15 bar) and CH_4 (1.4 bar) partial pressures were present in the reactor. For $\text{Pd}/\text{Al}_2\text{O}_3$, the presence of CO_2 and CH_4 has a negligible effect on productivity, yielding nearly identical values to those obtained under H_2/CO conditions. In contrast, for $\text{Pd-PO}_x\text{-1.7-600}/\text{Al}_2\text{O}_3$, the additional presence of CO_2 and CH_4 leads to a reduction in productivity by about one third compared to conditions with CO alone.

Temperature-programmed CO_2 hydrogenation

The catalysts were tested in a separate CO_2 hydrogenation reaction (without Hx-BT present) to further understand their interactions with H_2 , CO, CO_2 , and CH_4 . The results from experiments with $\text{Pd}/\text{Al}_2\text{O}_3$ and $\text{Pd-PO}_x\text{-1.7-600}/\text{Al}_2\text{O}_3$ at

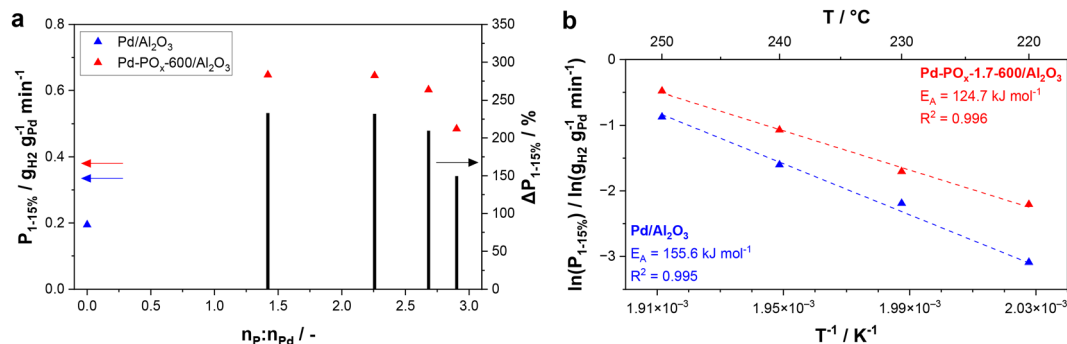


Fig. 3 H0-BT hydrogenation with H_2/CO , 30 bar H_2 -pressure and $n_{\text{Pd}} : n_{\text{H}_0\text{-BT}} = 5.1 \times 10^{-4}$. (a) $P_{1-15\%}$ of $\text{Pd}/\text{Al}_2\text{O}_3$ and $\text{Pd-PO}_x\text{-600}/\text{Al}_2\text{O}_3$ at 240 °C at different $n_P : n_{\text{Pd}}$ ratios (lot 2). (b) Arrhenius plot for $\text{Pd}/\text{Al}_2\text{O}_3$ (lot 4) and $\text{Pd-PO}_x\text{-1.7-600}/\text{Al}_2\text{O}_3$ ($n_P : n_{\text{Pd}} = 1.7 \pm 0.3$; lot 3) at 220–250 °C.

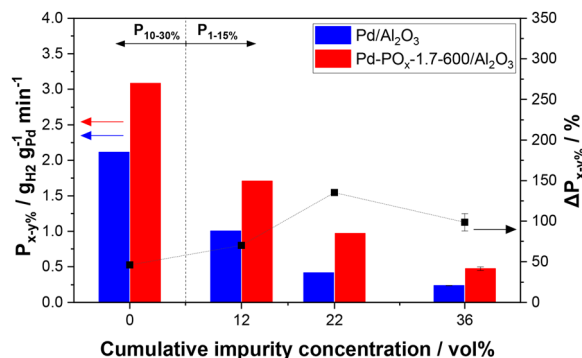


Fig. 4 H0-BT hydrogenation with H_2 /mixed at 240 °C and 30 bar H_2 -pressure. $P_{x-y\%}$ and $\Delta P_{x-y\%}$ of Pd/Al_2O_3 and $Pd-PO_x-1.7-600/Al_2O_3$ ($n_P : n_{Pd} = 1.7 \pm 0.3$) with $n_{Pd} : n_{H_0-BT} = 4.1 \times 10^{-4}$ (lot 2).

reaction temperatures ranging from 200 to 400 °C are shown in Fig. 5. Both catalysts exhibit negligible conversion at temperatures of 250 °C and below. At 400 °C, CO_2 conversion reaches 63% with Pd/Al_2O_3 , but only 20% with $Pd-PO_x-1.7-600/Al_2O_3$. Pd/Al_2O_3 shows a steadily decreasing CO selectivity with increasing temperatures. A CO selectivity below 3% is reached at 400 °C, indicating that most CO_2 is converted to CH_4 . The CO selectivity of $Pd-PO_x-1.7-600/Al_2O_3$ remains above 85% throughout the entire temperature range. Even at points of similar conversion, $Pd-PO_x-1.7-600/Al_2O_3$ shows constantly a much higher CO selectivity. These results suggest that PO_x modification reduces the catalyst's affinity to produce CH_4 from CO_2 and CO. Note that CO and CH_4 were the only identified products in both experiments.

Structural and morphological characterization

N_2 physisorption analysis was conducted and reveals that PO_x modification only has a negligible effect on pore size and surface area of the catalyst (Table S3 and Fig. S8). CO-pulse chemisorption was conducted for Pd/Al_2O_3 , $Pd-600/Al_2O_3$ and $Pd-PO_x-1.7-600/Al_2O_3$ (Table S4). The Pd dispersion of the commercial catalyst decreases from 18.5% (Pd/Al_2O_3) to 12.2% ($Pd-600/Al_2O_3$) after thermal treatment at 600 °C without

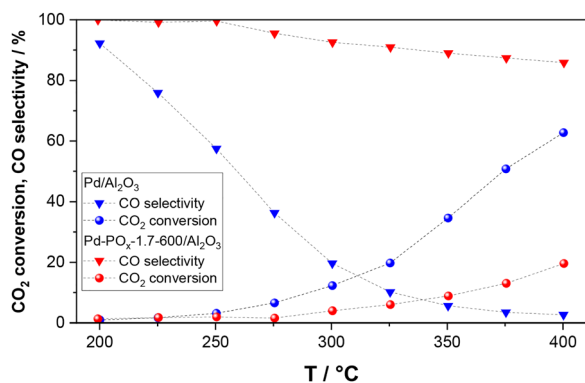


Fig. 5 CO_2 conversion and CO selectivity of Pd/Al_2O_3 and $Pd-PO_x-1.7-600/Al_2O_3$ over temperature during CO_2 hydrogenation with 0.5 g catalyst, a $H_2 : CO_2$ ratio of 4 : 1 and a GHSV of 2000 h^{-1} (lot 3).

previous PO_x modification. Similarly, the PO_x -modified catalyst with the highest activity in H0-BT hydrogenation ($Pd-PO_x-1.7-600/Al_2O_3$) shows a reduced dispersion of 13.0%.

To investigate the crystal structure of Pd and P, we performed XRD analysis on Pd/Al_2O_3 and $Pd-PO_x-1.7-600/Al_2O_3$. Note that the corresponding P-loading of approximately 2.2 wt% may be too low to detect crystalline phases of any formed structures. Therefore, we also analyzed $Pd-PO_x-5.1-600/Al_2O_3$, despite its low hydrogenation activity. The XRD patterns of all three samples exhibit reflections corresponding to metallic Pd^0 and $\gamma-Al_2O_3$ (Fig. 6). In fact, the patterns of Pd/Al_2O_3 and $Pd-PO_x-1.7-600/Al_2O_3$ are identical. Only the PO_x -modified sample with higher P-loading shows new signals attributed to $AlPO_4$. A crystalline species containing reduced phosphorus, like palladium phosphide, is not detected in the bulk of any sample (compare Fig. S1).

We investigated the Pd particle size of Pd/Al_2O_3 and $Pd-PO_x-600/Al_2O_3$ catalysts ($n_P : n_{Pd} = 0.7, 1.7, \text{ and } 3.7$) using HR-TEM (Fig. 7). Pd/Al_2O_3 exhibits an average Pd particle size of 5.8 nm, corresponding to a Pd dispersion of 14.7%. This value is in good agreement with the dispersion determined by CO-pulse chemisorption. This sample also shows a broad particle size distribution, as indicated by a large standard deviation of ± 2.2 nm. In contrast, PO_x -modification with varied $n_P : n_{Pd}$ ratios leads to a decrease in average nanoparticle size, narrower distributions and less tailing. $Pd-PO_x-0.7-600/Al_2O_3$ and $Pd-PO_x-3.7-600/Al_2O_3$ exhibit similar average particle sizes between 4.0 and 4.3 nm. For $Pd-PO_x-1.7-600/Al_2O_3$, the most active catalyst in hydrogenation, the smallest average Pd particle size of 3.6 nm is observed, corresponding to a theoretical Pd dispersion of 24.0%. This indicates an increase of $\sim 63\%$ in the number of Pd surface atoms compared to Pd/Al_2O_3 , which contrasts with the lower dispersion measured by CO-pulse chemisorption, as mentioned above. Note that Pd surface atoms that are potentially covered by PO_x cannot be identified in the HR-TEM images.

The two catalysts with the optimum $n_P : n_{Pd}$ ratio (1.6–1.7), subjected to thermal treatment at 500 °C and 700 °C, were also analyzed using HR-TEM (Fig. S9). Both show a reduction in average particle size compared to Pd/Al_2O_3 from 5.8 nm to 4.1 nm. However, the particle size decrease is not as

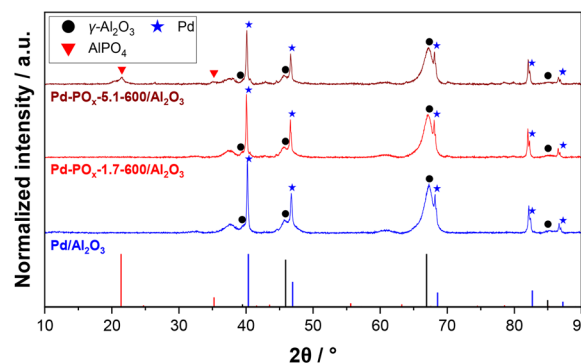


Fig. 6 XRD patterns of Pd/Al_2O_3 , $Pd-PO_x-1.7-600/Al_2O_3$ and $Pd-PO_x-5.1-600/Al_2O_3$ with Pd, $\gamma-Al_2O_3$ and $AlPO_4$ reference (lot 1 and 2).



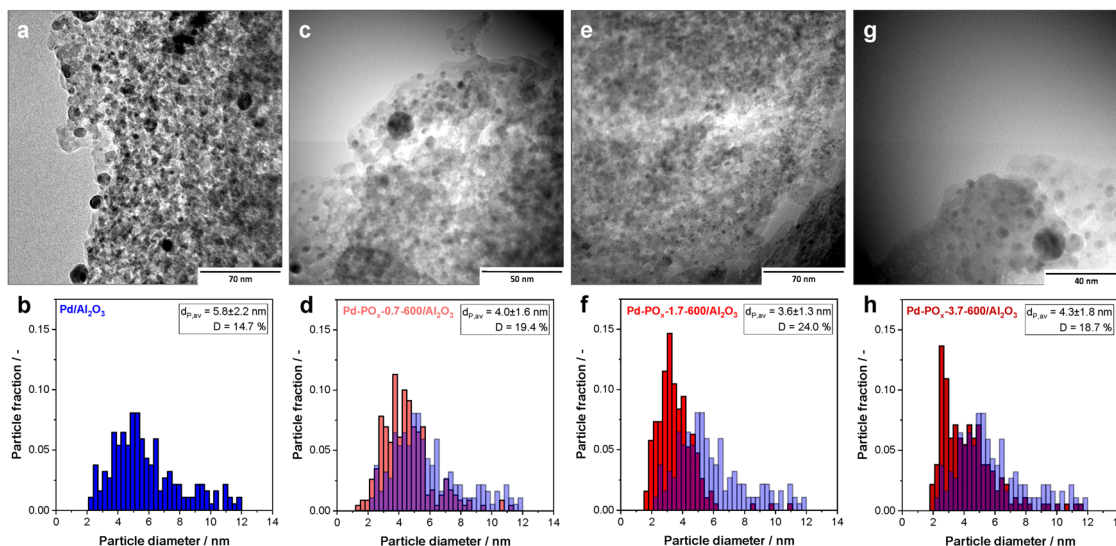


Fig. 7 HR-TEM and particle size distribution of (a) and (b) Pd/Al₂O₃, (c) and (d) Pd-PO_x-0.7-600/Al₂O₃, (e) and (f) Pd-PO_x-1.7-600/Al₂O₃ and (g) and (h) Pd-PO_x-3.7-600/Al₂O₃ (all lot 1).

pronounced compared to the PO_x-modified catalyst treated at 600 °C. It is interesting to note, that the catalyst treated at 700 °C is the PO_x-modified catalyst with the largest share of nanoparticles above 8 nm, despite its small average particle size (Fig. S10).

X-ray absorption spectroscopy

After assessing geometric effects due to PO_x modification, XANES at the Pd L₃-edge was used to probe the local electronic structure of Pd in Pd/Al₂O₃ and PO_x-modified catalysts. Pd L₃-edge XAS spectra of catalyst samples are compared to spectra measured on commercial Pd foil and PdO references (Fig. 8a). The edge positions of the reference compounds are 3172.6 eV for Pd foil and 3173.2 eV for PdO (Fig. S11a). Pd/Al₂O₃ and three Pd-PO_x-600/Al₂O₃ catalysts ($n_p:n_{Pd} = 1.2, 1.7, \text{ and } 2.1$) show identical edge positions (3172.9 eV; Fig. S11b) and line shapes, which also align well with previously reported spectra of *in situ* reduced Pd/Al₂O₃ catalysts.³⁴ This shows that PO_x modification has no significant influence on the electronic environment of Pd. Even though the catalysts were pre-reduced, the edge

positions, determined to lie between those observed for Pd foil and PdO, indicate the presence of Pd⁰ and positively charged Pd^{δ+} species. These Pd^{δ+} species can be attributed to Pd atoms at the interface between Pd nanoparticles and the Al₂O₃ support. Furthermore, the increased white line intensity of the catalysts compared to Pd foil is attributed to the high fraction of undercoordinated Pd atoms in the nanoparticles, which is associated with a greater number of unoccupied 4d-states.³⁴

The same catalysts were further analyzed by EXAFS at the Pd L₂-edge to investigate the coordination environment of Pd in the PO_x-modified catalysts. The corresponding Fourier-transformed spectra in *R*-space are shown in Fig. 8b, while the normalized spectra and the *k*²-weighted EXAFS data in *k*-space are provided in Fig. S12 and S13, respectively. The PdO reference exhibits a dominant peak at 1.4 Å, corresponding to Pd-O coordination, and a second feature at 3.2 Å, which can be assigned to Pd-Pd coordination (distances phase-uncorrected). In the spectrum of the Pd foil, a main peak appears at 2.8 Å, consistent with Pd-Pd coordination, along with a minor feature at around 1.8 Å. The Pd₃P/SiO₂ reference sample

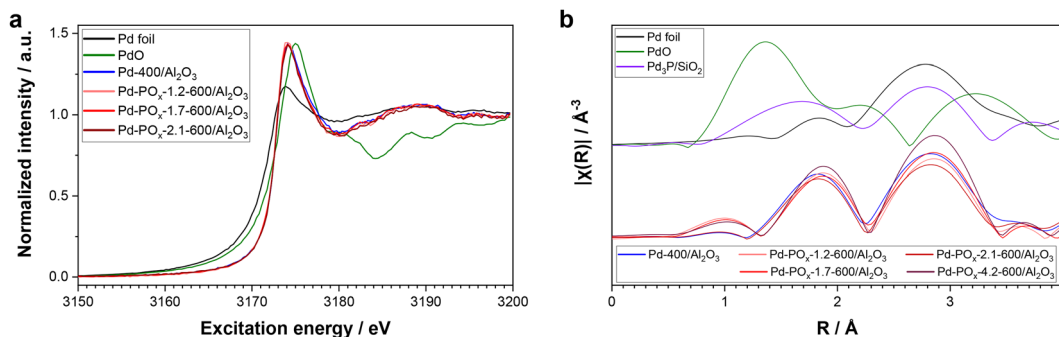


Fig. 8 (a) Normalized Pd L₃-edge XANES spectra and (b) Fourier-transformed Pd L₂-edge EXAFS spectra (*k*²-weighted, *R*-space) of Pd foil, PdO, Pd-400/Al₂O₃, Pd-PO_x-1.2-600/Al₂O₃, Pd-PO_x-1.7-600/Al₂O₃, Pd-PO_x-2.1-600/Al₂O₃ and Pd-PO_x-4.2-600/Al₂O₃ (lot 2).



Table 1 Results of EXAFS fitting: energy shift (ΔE_0), R -factor, interatomic distances (r) and coordination numbers (CN) for Pd–Pd and Pd–O paths. The Debye–Waller factor (σ^2) is reported for the Pd–Pd path; for Pd–O, σ^2 was fitted for PdO (0.0036 Å²) and fixed for all other samples (0.007 Å²) due to the low CN

	$\Delta E_0/\text{eV}$	$R\text{-factor}/\%$	Pd–Pd			Pd–O	
			$r/\text{\AA}$	CN	$\sigma^2/\text{\AA}^2 \cdot 10^{-3}$	$r/\text{\AA}$	CN
Pd-400/Al ₂ O ₃	5.8 ± 1.6	3.4	2.72	9.8 ± 2.4	7.2 ± 3.8	1.89	0.9 ± 0.5
Pd-PO _x -1.2-600/Al ₂ O ₃	6.8 ± 1.8	4.8	2.73	6.9 ± 2.0	3.1 ± 3.9	1.88	0.8 ± 0.5
Pd-PO _x -1.7-600/Al ₂ O ₃	6.8 ± 1.1	2.0	2.73	7.9 ± 1.4	4.1 ± 2.5	1.89	0.7 ± 0.3
Pd-PO _x -2.1-600/Al ₂ O ₃	5.7 ± 1.7	4.4	2.72	6.9 ± 1.9	4.3 ± 3.8	1.89	0.9 ± 0.5
Pd-PO _x -4.2-600/Al ₂ O ₃	6.8 ± 1.1	1.8	2.73	7.2 ± 1.3	0.1 ± 2.3	1.89	0.7 ± 0.4
Pd foil	5.3 ± 2.2	8.4	2.72	12.6 ± 4.1	13.9 ± 5.7	—	—
PdO	0.0 ± 1.3	6.0	3.33	8.0	3.0 ± 3.9	1.91	4.0

(see corresponding XRD pattern in Fig. S1) shows a reduced Pd–Pd coordination intensity at the same distance as in metallic Pd, along with an additional feature at approximately 1.6 Å, which we attribute to Pd–P coordination. All references are in good agreement with previous reports.^{35–37} The catalyst samples show a pronounced peak at 2.8–2.9 Å, the distance characteristic of metallic Pd–Pd coordination. In addition, another peak is observed at 1.8–1.9 Å, which is more intense than in the Pd foil reference. This feature has previously been attributed to Pd atoms coordinated to oxygen species from the Al₂O₃ support (Pd–O_{Al}).³⁸ Notably, the feature at 1.8–1.9 Å is observed in all PO_x-modified catalysts and closely resembles that of the unmodified Pd/Al₂O₃, showing only minor shifts in position and intensity without a clear trend. As the unmodified catalyst contains no P and thus cannot exhibit Pd–P coordination, and given the spectral similarity in this region across all samples, we exclude the presence of direct Pd–P interactions in the PO_x-modified catalysts.

For quantitative analysis, we performed EXAFS fitting, with the resulting parameters summarized in Table 1 and the corresponding fits shown in Fig. S14. All catalysts show significant Pd–Pd coordination, with a coordination number of approximately 9.8 for Pd/Al₂O₃ and consistently lower values between 6.9 and 7.9 for the PO_x-modified catalysts. This trend is consistent with the decrease in particle size upon PO_x modification observed *via* HR-TEM.³⁹ In addition, all samples show low Pd–O coordination numbers ranging from 0.7 to 0.9, which we attribute to Pd–O_{Al} coordination. Notably, the PO_x-modified catalysts exhibit consistently smaller Debye–Waller factors for the Pd–Pd path, indicating reduced structural disorder in the Pd nanoparticles compared to Pd/Al₂O₃. This finding is particularly unexpected, as smaller nanoparticles typically exhibit higher Debye–Waller factors due to increased structural disorder. This may point to a PO_x-induced increase in metal–support interaction (MSI) from weak to moderate, leading to more ordered Pd nanoparticles.⁴⁰

The electronic environment of P in PO_x-modified catalysts was probed using XANES at the P K-edge (Fig. 9). Reference compounds, including H₃PO₃, H₃PO₄ and AlPO₄, were analyzed alongside two PO_x-modified catalysts with different $n_{\text{P}}:n_{\text{Pd}}$ ratios, corresponding to varying P-loadings. H₃PO₃, which contains P³⁺ and served as the P-precursor during catalyst synthesis, exhibits an edge position at 2149.5 eV (Fig. S15a).

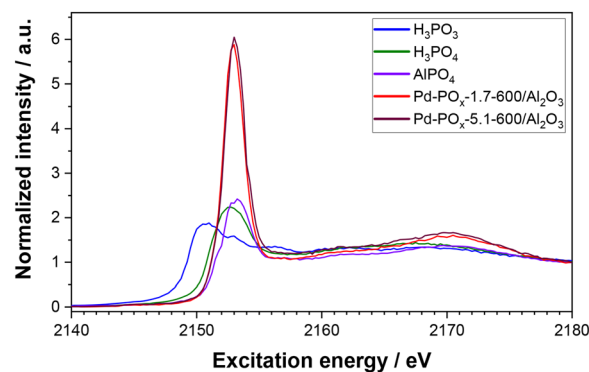


Fig. 9 Normalized P K-edge XANES spectra of H₃PO₃, H₃PO₄, AlPO₄, Pd-PO_x-1.7-600/Al₂O₃ and Pd-PO_x-5.1-600/Al₂O₃ (lot 2).

H₃PO₄ and AlPO₄, both containing P⁵⁺, show edge positions at 2151.0 eV and 2152.3 eV, respectively. Both PO_x-modified catalysts exhibit edge positions at 2152.3 eV, closely aligned with that of AlPO₄, indicating that P in these materials is predominantly in the 5+ oxidation state. Further, all reference compounds and PO_x-modified catalysts show a broader secondary feature at ~2170 eV, attributed to oxygen oscillation, a characteristic commonly observed in phosphates.^{41,42} Furthermore, the white line intensities for PO_x-modified catalysts are more than twofold higher, compared to AlPO₄. In line with literature, we attribute this to a high abundance of monomeric and highly dispersed phosphate species on the Al₂O₃ support.^{43–45} Notably, Pd-PO_x-5.1-600/Al₂O₃ reveals a subtle shift in its white line peak of ~0.14 ± 0.03 eV compared to Pd-PO_x-1.7-600/Al₂O₃ as can be seen in Fig. S15b. In combination with previously discussed XRD results (see Fig. 6), we attribute this white line shift of the catalyst with high P-loading towards the white line position of AlPO₄ to an increasing fraction of polymeric phosphates and crystalline AlPO₄.

Temperature-programmed desorption of NH₃ and CO

To study the effect of PO_x modification on the surface acidity of the support, we performed NH₃-TPD (Fig. 10a). The TCD signal of the unmodified catalyst shows a broad peak at 151 °C, followed by a gradual decline in intensity. Both PO_x-modified catalysts exhibited a shoulder in the temperature range of 130 to 135 °C and a pronounced peak at 190 °C and 197 °C for the



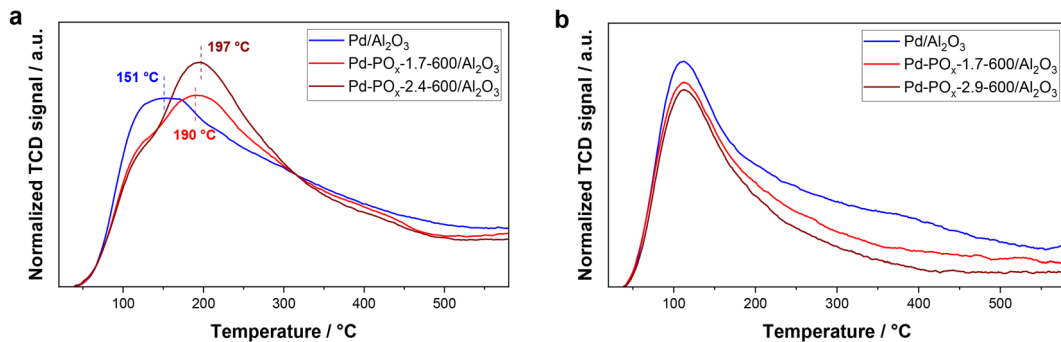


Fig. 10 (a) NH_3 -TPD of $\text{Pd}/\text{Al}_2\text{O}_3$ (lot 4), $\text{Pd}-\text{PO}_x-1.7-600/\text{Al}_2\text{O}_3$ and $\text{Pd}-\text{PO}_x-2.4-600/\text{Al}_2\text{O}_3$ (lot 2). (b) CO -TPD of $\text{Pd}/\text{Al}_2\text{O}_3$, $\text{Pd}-\text{PO}_x-1.7-600/\text{Al}_2\text{O}_3$ and $\text{Pd}-\text{PO}_x-2.9-600/\text{Al}_2\text{O}_3$ (lot 2).

catalysts with molar P : Pd ratio of 1.7 and 2.4, respectively. The peak intensities of $\text{Pd}/\text{Al}_2\text{O}_3$ and $\text{Pd}-\text{PO}_x-1.7-600/\text{Al}_2\text{O}_3$ are comparable. In contrast, $\text{Pd}-\text{PO}_x-2.4-600/\text{Al}_2\text{O}_3$ exhibits a distinct increase in peak intensity. NH_3 desorption around 150 °C is attributed to weak acid sites, while desorption near 200 °C indicates the presence of moderate acid sites.⁴⁶ TCD signals at temperatures above 300 °C, attributed to strong acid sites,⁴⁶ are identical for all catalysts. In summary, PO_x modification increases both the number and strength of acid sites on the Al_2O_3 support.

Furthermore, we performed CO -TPD to investigate the interaction of CO with $\text{Pd}/\text{Al}_2\text{O}_3$, $\text{Pd}-\text{PO}_x-1.7-600/\text{Al}_2\text{O}_3$ and $\text{Pd}-\text{PO}_x-2.9-600/\text{Al}_2\text{O}_3$ (Fig. 10b). All catalysts exhibit a distinct peak around 112 °C, corresponding to weakly bound CO ,⁴⁷ with $\text{Pd}/\text{Al}_2\text{O}_3$ showing a slightly higher intensity than the PO_x -modified samples. The absence of a temperature shift indicates that the intrinsic $\text{Pd}-\text{CO}$ binding strength remains largely unaffected by PO_x modification. Desorption of more strongly bound CO from $\text{Pd}(111)$ facets has been shown to occur above 160 °C.⁴⁸ In this range, the CO desorption signal of $\text{Pd}/\text{Al}_2\text{O}_3$ clearly exceeds that of the PO_x -modified catalysts, indicating a greater proportion of (111) facets in the unmodified sample.

Temperature-programmed CO-DRIFTS

To further study the CO interaction and differentiate between the available Pd adsorption sites on $\text{Pd}/\text{Al}_2\text{O}_3$ and $\text{Pd}-\text{PO}_x/\text{Al}_2\text{O}_3$, we applied temperature-programmed CO -DRIFTS. We focused on the temperature range between room temperature and reaction temperature of 240 °C. The stretching frequency of CO adsorbates, $\nu(\text{CO})$, on metal surfaces is highly sensitive to the binding site, adsorption motif, electronic properties of the metal, and the presence of co-adsorbates.^{49–51} Fig. 11 shows selected spectra during heating and cooling of $\text{Pd}/\text{Al}_2\text{O}_3$ and $\text{Pd}-\text{PO}_x-1.7-600/\text{Al}_2\text{O}_3$ in 1 bar CO . Overall, peaks are more intense for $\text{Pd}/\text{Al}_2\text{O}_3$, though comparisons of absolute values across different DRIFTS experiments should be done with caution. The topmost spectrum was recorded at room temperature. Here, we observe pronounced peaks at 2093/2098 and 1985 cm^{-1} on both samples, while only $\text{Pd}/\text{Al}_2\text{O}_3$ exhibits a peak at the lower frequency of 1938 cm^{-1} . For $\text{Pd}-\text{PO}_x-1.7-600/\text{Al}_2\text{O}_3$, the broad peak at 1985 cm^{-1} is highly asymmetrical,

indicating that the feature at 1938 cm^{-1} contributes to this broad band.

These findings are in good agreement with a previous contribution from some of us, which we rationalize accordingly.⁵² In brief, we apply a surface science approach where nanoparticles are considered as entities with distinct contributions of crystal facets as well as edges and corners. For Pd , the most stable and, thus, abundant facets are of the (111) and (100) orientations.⁵³ We assign the band at 2090–2100 cm^{-1} to $\nu(\text{CO})$ of adsorbates in on-top configuration on both facets and on low-coordinated Pd atoms.^{54–57} We attribute the peak at 1985 cm^{-1} to CO in bridge configuration at edge sites, with a minor contribution from bridge CO at defect sites and on $\text{Pd}(100)$.^{57–59} The band at 1938 cm^{-1} results from coupling between CO adsorbates in bridge and three-fold hollow configuration on $\text{Pd}(111)$ terraces.^{55,60} It is important to note that these three types of CO adsorbates are found on both samples, albeit to varying degrees. The suppression of the latter signal in the spectrum of $\text{Pd}-\text{PO}_x-1.7-600/\text{Al}_2\text{O}_3$ indicates the formation and stabilization of smaller Pd nanoparticles with less extended facets.^{55,61} This is in good agreement with the already discussed particle size decrease observed *via* HR-TEM and EXAFS analyses. Furthermore, the fact PO_x modification does not induce pronounced change in the absolute band positions indicates that the Pd binding partners experience similar electronic environments in both samples. This is in excellent agreement with the results from X-ray absorption spectroscopy and CO -TPD.

As the temperature increases to 240 °C, we observe an intensity loss and a shift of the bands toward lower wavenumbers for both samples, with the extent of the shift being almost identical (~ 15 to 20 cm^{-1}). This shift and intensity reduction are due to partial CO desorption with increasing temperature, leading to a lower amount of dipole coupling. Desorption is most pronounced for the weakly bound on-top CO . However, our results show that the majority of CO remains adsorbed on all samples even at reaction temperature. Unmodified $\text{Pd}/\text{Al}_2\text{O}_3$ shows a significant contribution of $\text{Pd}(111)$ facets (peak at 1915 cm^{-1}) at 240 °C. In contrast, for $\text{Pd}-\text{PO}_x-1.7/\text{Al}_2\text{O}_3$ the band at ~ 1970 cm^{-1} , associated with steps and edges, is the most intense. Upon cooling back to room temperature,



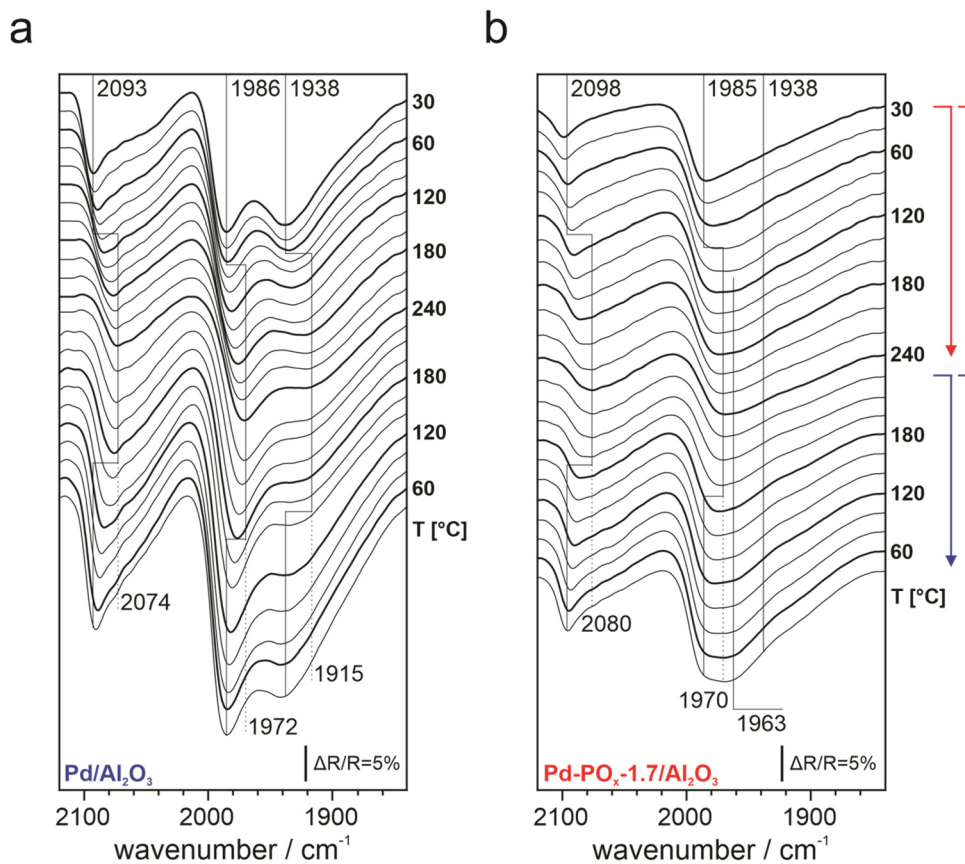


Fig. 11 CO-DRIFT spectra recorded during temperature-programmed experiments with (a) Pd/Al₂O₃ and (b) Pd-PO_x-1.7-600/Al₂O₃ (lot 3).

the band shift reverse, and all peaks return to their original positions, with only slight changes in the relative intensity of the bands.

Discussion

PO_x modification of Pd/Al₂O₃ leads to an increase in the apparent catalytic activity for the hydrogenation of benzyltoluene under pure hydrogenation of up to 60%. The following section aims to discuss possible structural and electronic reasons for this enhancement, based on detailed material characterization.

To address this, we examined the chemical nature of phosphorus in the modified Pd/Al₂O₃ catalyst. XRD and EXAFS analyses confirm the absence of Pd phosphides at both optimal and high P-loadings. This behavior on Al₂O₃ is distinct from that observed with SiO₂ (Fig. S1), TiO₂,⁶² and carbon⁶³ where phosphides typically form under similar synthesis conditions. Instead, at ideal P-loadings we observe monomeric and highly dispersed phosphate species on the Al₂O₃ support with XANES analysis. At excessive P-loadings, this ultimately leads to the formation of crystalline AlPO₄.

The observed activity increase during H₀-BT hydrogenation is unlikely to result from electronic modification of Pd. This is supported by analyses using (1) XANES, (2) CO-DRIFTS and (3)

CO-TPD, all showing that the Pd oxidation state and local electronic environment remain unchanged upon PO_x modification. Moreover, the unchanged apparent activation energies in H₀-BT hydrogenation with pure H₂ confirm that the intrinsic activity of Pd⁰ is preserved and the general hydrogenation mechanism remains unchanged. Instead, the formation of a Pd-phosphide phase on other supports, *e.g.*, SiO₂, leads to a modification of the active site and a decrease in activity compared to Pd⁰.

Since a change in the identity of the active site can most likely be excluded, the enhanced catalytic productivity is more plausibly attributed to a higher abundance of active sites. Our HR-TEM results highlight that PO_x modification induces a redispersion of Pd nanoparticles, leading to a reduction in the average particle size from 5.8 to 3.6 nm in the catalyst with the highest hydrogenation activity. Additionally, EXAFS fitting revealed consistently smaller Pd-Pd coordination numbers for PO_x-modified catalysts compared to Pd/Al₂O₃, supporting the theory of smaller particles. This translates to a geometric effect, *i.e.*, the NPs expose fewer terrace sites and more edge sites in the PO_x-modified samples. Our CO-DRIFTS results indicate that this is preserved at reaction temperature.

To gain insight into the origin of this redispersion effect, we systematically varied the thermal treatment temperature and observed a pronounced temperature dependence.



A temperature of 600 °C appears optimal, coinciding with the highest dispersion and activity. Consequently, we suspect that enhanced Pd mobility at elevated temperature is required for optimal redispersion. At higher temperatures, however, a bimodal size distribution emerges, suggesting that sintering begins to outweigh redispersion as the Tammann temperature of Pd (641 °C⁶⁴) is approached. Nevertheless, the formation and stabilization of small Pd particles even after thermal treatment at 600 °C underscores the high stability against sintering of the PO_x-modified catalysts.

In addition to the thermal treatment temperature, the $n_p:n_{pd}$ ratio plays a critical role in achieving optimal Pd dispersion and catalytic activity, as shown by the volcano-type productivity plot. Without PO_x, thermal treatment at 600 °C promotes sintering, reduces Pd dispersion and hampers productivity. An intermediate $n_p:n_{pd}$ ratio (1.7 ± 0.3) likely optimizes hydrogenation activity, because well-dispersed PO_x species modify the chemical nature of the Al₂O₃ support and enhance metal-support interaction. This interpretation is supported by the observed reduction in the Debye-Waller factor upon PO_x modification, indicating decreased structural disorder in the Pd nanoparticles. The resulting stronger interaction with the support facilitates redispersion and promotes the stabilization of redistributed Pd particles. At higher $n_p:n_{pd}$ ratios, however, previously discussed crystalline AlPO₄ further modifies the properties of the support surface in a way that adversely affects Pd dispersion and catalytic activity. Moreover, excessive P-loading is likely to cause increased site blocking of active Pd species by PO_x or AlPO₄, further contributing to the decline in activity.

While HR-TEM, CO-DRIFTS and EXAFS reveal higher dispersion after PO_x modification, CO-pulse chemisorption indicates a decrease in accessible Pd sites. This apparent contradiction is resolved by our recent study, which shows that PO_x-induced site blocking is largely reversible under our reaction conditions.⁵² As this restores the accessibility of blocked Pd sites, we expect the dispersion increase quantified *via* HR-TEM to be fully available for catalysis. In the current study, the Pd dispersions from HR-TEM increase from 14.7% to 24.0% upon PO_x modification, corresponding to a relative improvement of ~63% for the most active Pd-PO_x/Al₂O₃ catalyst. This enhanced dispersion is consistent with the productivity gain of 40 to 60% under pure H₂. This observation aligns with the structure-insensitive nature of aromatic hydrogenation with pure H₂ over Pd,^{65–68} reinforcing that the increased number of active sites, instead of changes in their chemical nature, is responsible for the enhanced activity.

The second question addressed in this study concerns the effect of PO_x modification on the CO poisoning tolerance during H₀-BT hydrogenation. Our catalytic data clearly demonstrate that PO_x modification enhances the CO poisoning tolerance of the Pd/Al₂O₃ catalyst when operating with impure H₂ feed. This is evidenced by a significantly higher relative productivity increase under H₂/CO conditions of up to 230%.

One contributing factor to the improved CO tolerance is the increased surface acidity of the Al₂O₃ support, as evidenced by

NH₃-TPD. Acid sites in close proximity to noble metal particles are known to serve as active sites for aromatic hydrogenation with spilled-over hydrogen.^{69–73} While their contribution under pure H₂ is likely limited, it becomes more relevant under H₂/CO conditions, as these sites are not susceptible to CO poisoning. Notably, hydrogenation with pure H₂ shows a similar temperature dependence on both acid sites and Pd.^{69,70} Since hydrogenation over acid sites is expected to be less affected by CO, this effect may help explain the lower apparent activation energy observed for Pd-PO_x/Al₂O₃ compared to Pd/Al₂O₃ under H₂/CO conditions. However, given the moderate increase in surface acidity, it is unlikely to be the main reason for the enhanced CO tolerance.

The improved CO tolerance also correlates with CO-TPD measurements, which reveal a reduction of strongly bound CO species on the PO_x-modified catalyst. Complementary CO-DRIFTS data and literature reports indicate that these strongly bound species predominantly occupy bridge and three-fold hollow sites on Pd terrace atoms.⁴⁸ Their reduction upon PO_x modification is thus consistent with the previously discussed PO_x-induced redispersion.

To further support this interpretation, we investigated CO₂ hydrogenation as a probe reaction, with a special focus on the fate of CO formed *via* the RWGS reaction. For the PO_x-modified catalyst, CO desorbs readily from abundant and comparatively weakly binding Pd edge sites, leading to a CO selectivity above 80%. In contrast, on unmodified Pd/Al₂O₃, where terrace sites dominate, stronger CO adsorption facilitates hydrogenation to CH₄. This size-dependent CO hydrogenation selectivity also accounts for the greater susceptibility of the PO_x-modified catalyst to CO₂-rich feeds during benzyltoluene hydrogenation, as elevated CO₂ concentrations promote CO formation.

We propose that benzyltoluene hydrogenation under CO-containing H₂ proceeds preferentially at Pd edge sites. We base this hypothesis on the increased density in edge sites, where CO binds more weakly,^{74,75} and benzene, a similar aromatic compound, was shown to preferentially adsorb in the presence of CO.⁷⁶ This provides a mechanistic rationale for the observed productivity increase under impure H₂, which is disproportional to the dispersion increase, and cannot be explained by a change in electronic properties of Pd or altered Pd-CO interaction. Building on these findings, we aim to further explore the ability of CO to induce structure sensitivity in Pd-catalyzed aromatic hydrogenation and to leverage this understanding to maximize catalytic activity through rational catalyst design.

Conclusion

Phosphate modification of Pd/Al₂O₃ enhances catalytic activity in benzyltoluene hydrogenation, increasing productivity by 60% under pure H₂ and by 230% under CO-contaminated H₂. PO_x modification induces increased stability against sintering and Pd redispersion, yielding smaller nanoparticles through a combination of enhanced Pd mobility during high temperature thermal treatment and altering of the metal-support



interaction by highly dispersed phosphate species on Al₂O₃. Importantly, PO_x modification does not lead to a significant electronic modification of Pd⁰, as confirmed by spectroscopic characterization. The productivity increase under pure H₂ reflects the structure-insensitive nature of aromatic hydrogenation and correlates with the increased Pd dispersion. Under CO-contaminated H₂, CO induces structure sensitivity, favoring benzyltoluene hydrogenation at Pd edge sites over terrace sites, explaining the significantly higher productivity increase. Stronger and more abundant acid sites introduced by PO_x modification further enhance productivity under CO-contaminated conditions, as they provide additional sites for aromatic hydrogenation with spilled-over hydrogen that are not susceptible to CO poisoning.

Author contributions

During the preparation of this work the authors used ChatGPT in order to improve the language. After using this tool/service, the authors reviewed and edited the content as needed and take full responsibility for the content of the publication.

Conflicts of interest

The authors declare no conflict of interest.

Data availability

Research data to this article can be found online at <https://doi.org/10.5281/zenodo.16454174>.

Supplementary information (SI) is available. See DOI: <https://doi.org/10.1039/d5ey00231a>.

Acknowledgements

We gratefully acknowledge the Federal Ministry of Research, Technology and Space for funding of the BMFTR Junior Research Group FAIR-H2 (Grant number (FKZ): 03SF0730). We thank the Helmholtz-Zentrum Berlin für Materialien und Energie for the allocation of synchrotron radiation beamtime at the HiKE endstation located at the KMC-1 beamline and the Energy Materials In Situ Laboratory Berlin (EMIL) for providing access to facilities allowing for on-site sample mounting in inert (Ar) atmosphere. Y. S. and T. R. acknowledge funding by the Deutsche Forschungsgemeinschaft (DFG, German Research Foundation): Project-ID 431791331, SFB 1452 (CLINT Catalysis at Liquid Interfaces) and Project-ID 530732852. We thank the Center for Nanoanalysis and Electron Microscopy (CENEM) Erlangen for providing the HR-TEM facility. We thank Yousuf Raed Ramzi (HR-TEM), Abelina Ellert (ICP-OES), Ana de Oliveira (ICP-OES), Lukas Popp (N₂ physisorption), Susanne Pachaly (XRD), Jiaqi Xiao and Felix Lott for experimental support.

References

- 1 R. Noyori, Catalytic Hydrogenation: A Core Technology in Synthesis, *Adv. Synth. Catal.*, 2003, **345**(1–2), 1, DOI: [10.1002/adsc.200390012](https://doi.org/10.1002/adsc.200390012).
- 2 *Catalysis without Precious Metals*, ed. R. M. Bullock, Wiley-VCH, Weinheim, 2010.
- 3 S. Li, L. Lin, Z. Wang and D. Ma, Direct Utilization of Crude and Waste H₂ via CO-Tolerant Hydrogenation, *Innovation*, 2023, **4**(1), 100353, DOI: [10.1016/j.xinn.2022.100353](https://doi.org/10.1016/j.xinn.2022.100353).
- 4 T. Suzuki, H. Sekine, M. Ohshima, H. Kurokawa and H. Miura, Hydrogenation of Naphthalene and Tetralin in the Presence of CO over Various Supported Metal Catalysts, *Kagaku Kogaku Ronbunshu*, 2007, **33**(6), 593–598, DOI: [10.1252/kakoronbunshu.33.593](https://doi.org/10.1252/kakoronbunshu.33.593).
- 5 H. Jorschick, *Ein-Reaktor-Konzept Und Mischgashydrierung Als Verfahrensvarianten Zur Effizienzsteigerung in Der LOHC-Basierten Wasserstoffspeicherung*, Friedrich-Alexander-Universität Erlangen-Nürnberg, 2019.
- 6 J. Spielmann, F. Buch and S. Harder, Early Main-Group Metal Catalysts for the Hydrogenation of Alkenes with H₂, *Angew. Chem.*, 2008, **120**(49), 9576–9580, DOI: [10.1002/ange.200804657](https://doi.org/10.1002/ange.200804657).
- 7 P. Preuster, C. Papp and P. Wasserscheid, Liquid Organic Hydrogen Carriers (LOHCs): Toward a Hydrogen-Free Hydrogen Economy, *Acc. Chem. Res.*, 2017, **50**(1), 74–85, DOI: [10.1021/acs.accounts.6b00474](https://doi.org/10.1021/acs.accounts.6b00474).
- 8 H. Jorschick, P. Preuster, A. Bösmann and P. Wasserscheid, Hydrogenation of Aromatic and Heteroaromatic Compounds – a Key Process for Future Logistics of Green Hydrogen Using Liquid Organic Hydrogen Carrier Systems, *Sustainable Energy Fuels*, 2021, **5**(5), 1311–1346, DOI: [10.1039/D0SE01369B](https://doi.org/10.1039/D0SE01369B).
- 9 F. Auer, D. Blaumeiser, T. Bauer, A. Bösmann, N. Szesni, J. Libuda and P. Wasserscheid, Boosting the Activity of Hydrogen Release from Liquid Organic Hydrogen Carrier Systems by Sulfur-Additives to Pt on Alumina Catalysts, *Catal. Sci. Technol.*, 2019, **9**(13), 3537–3547, DOI: [10.1039/C9CY00817A](https://doi.org/10.1039/C9CY00817A).
- 10 A. Zilm, F. Ortner, F. Gackstatter, S. Köberlein, J. Kadar, M. Geißelbrecht, A. Bösmann and P. Wasserscheid, Impurities in Hydrogen Released from Perhydro Benzyltoluene – Assessment and Adsorptive Removal, *Int. J. Hydrogen Energy*, 2025, **101**, 469–481, DOI: [10.1016/j.ijhydene.2024.12.204](https://doi.org/10.1016/j.ijhydene.2024.12.204).
- 11 H. Sekine, M. Ohshima, H. Kurokawa and H. Miura, Liquid Phase Hydrogenation of Naphthalene in the Presence of CO over Supported Ni Catalyst, *React. Kinet. Catal. Lett.*, 2008, **95**(1), 99–105, DOI: [10.1007/s11144-008-5295-5](https://doi.org/10.1007/s11144-008-5295-5).
- 12 Z. Wang, C. Dong, X. Tang, X. Qin, X. Liu, M. Peng, Y. Xu, C. Song, J. Zhang, X. Liang, S. Dai and D. Ma, CO-Tolerant RuNi/TiO₂ Catalyst for the Storage and Purification of Crude Hydrogen, *Nat. Commun.*, 2022, **13**(1), 4404, DOI: [10.1038/s41467-022-32100-x](https://doi.org/10.1038/s41467-022-32100-x).
- 13 S. Dürr, M. Müller, H. Jorschick, M. Helmin, A. Bösmann, R. Palkovits and P. Wasserscheid, Carbon Dioxide-Free



- Hydrogen Production with Integrated Hydrogen Separation and Storage, *ChemSusChem*, 2017, **10**(1), 42–47, DOI: [10.1002/cssc.201600435](https://doi.org/10.1002/cssc.201600435).
- 14 H. Jorschick, A. Bösmann, P. Preuster and P. Wasserscheid, Charging a Liquid Organic Hydrogen Carrier System with H₂/CO₂ Gas Mixtures, *ChemCatChem*, 2018, **10**(19), 4329–4337, DOI: [10.1002/cctc.201800960](https://doi.org/10.1002/cctc.201800960).
 - 15 H. Jorschick, M. Vogl, P. Preuster, A. Bösmann and P. Wasserscheid, Hydrogenation of Liquid Organic Hydrogen Carrier Systems Using Multicomponent Gas Mixtures, *Int. J. Hydrogen Energy*, 2019, **44**(59), 31172–31182, DOI: [10.1016/j.ijhydene.2019.10.018](https://doi.org/10.1016/j.ijhydene.2019.10.018).
 - 16 A. A. Taimoor, I. Pitault and F. C. Meunier, Correlation between Deactivation and Pt-Carbonyl Formation during Toluene Hydrogenation Using a H₂/CO₂ Mixture, *J. Catal.*, 2011, **278**(1), 153–161, DOI: [10.1016/j.jcat.2010.12.002](https://doi.org/10.1016/j.jcat.2010.12.002).
 - 17 J. Scalbert, C. Daniel, Y. Schuurman, C. Thomas and F. C. Meunier, Rational Design of a CO₂-Resistant Toluene Hydrogenation Catalyst Based on FT-IR Spectroscopy Studies, *J. Catal.*, 2014, **318**, 61–66, DOI: [10.1016/j.jcat.2014.07.013](https://doi.org/10.1016/j.jcat.2014.07.013).
 - 18 A. Neyyathala, F. Flecken and S. Hanf, A Supported Palladium Phosphide Catalyst for the Wacker–Tsuji-Oxidation of Styrene, *ChemPlusChem*, 2023, **88**(2), e202200431, DOI: [10.1002/cplu.202200431](https://doi.org/10.1002/cplu.202200431).
 - 19 L. Popp, P. Kampe, B. Fritsch, A. Hutzler, M. J. Poller, J. Albert and P. Schühle, Supported Ruthenium Phosphide as a Promising Catalyst for Selective Hydrogenation of Sugars, *Eur. J. Inorg. Chem.*, 2024, (22), e202400117, DOI: [10.1002/ejic.202400117](https://doi.org/10.1002/ejic.202400117).
 - 20 R. Stöber, F. Mai, O. Sebastian, A. Körner, A. Hutzler and P. Schühle, A Highly Stable Bimetallic Transition Metal Phosphide Catalyst for Selective Dehydrogenation of *N*-Heptane, *ChemCatChem*, 2022, **14**(18), e202200371, DOI: [10.1002/cctc.202200371](https://doi.org/10.1002/cctc.202200371).
 - 21 B. Liu, X. Lan, Q. Zhong and T. Wang, Metal Phosphide: An Atypical Catalytic Site, *ACS Catal.*, 2024, 757–775, DOI: [10.1021/acscatal.3c05160](https://doi.org/10.1021/acscatal.3c05160).
 - 22 L. Alvarado Rupflin, C. Boscagli and S. Schunk, Platinum Group Metal Phosphides as Efficient Catalysts in Hydroprocessing and Syngas-Related Catalysis, *Catalysts*, 2018, **8**(3), 122, DOI: [10.3390/catal8030122](https://doi.org/10.3390/catal8030122).
 - 23 J. Oh, N. Jeon, I. Chung, O. Seo, J. Park, A. Tayal and Y. Yun, P-Modified Pt/Al₂O₃ Catalysts for Selective Propane Dehydrogenation, *Appl. Catal., A*, 2024, 119783, DOI: [10.1016/j.apcata.2024.119783](https://doi.org/10.1016/j.apcata.2024.119783).
 - 24 A. Ellert, F. Herold, M. Rønning, A. Hutzler, L. Piccirilli, T. V. W. Janssens, P. N. R. Vennestrøm, P. Wasserscheid and P. Schühle, Phosphorus-Modification of Pt/Al₂O₃ Catalysts Improves Dispersion and Cycloalkane Dehydrogenation Activity, *J. Catal.*, 2024, **436**, 115607, DOI: [10.1016/j.jcat.2024.115607](https://doi.org/10.1016/j.jcat.2024.115607).
 - 25 A. Ellert, F. Ding, A. Hutzler, F. Herold, L. Piccirilli, M. Rønning, T. V. W. Janssens, D. Wisser and P. Schühle, Solvent-Free Phosphorus Modification of Pt/Al₂O₃ Catalysts to Improve Dispersion and Dehydrogenation Activity, *Appl. Catal., A*, 2025, **696**, 120199, DOI: [10.1016/j.apcata.2025.120199](https://doi.org/10.1016/j.apcata.2025.120199).
 - 26 R. Stöber, F. Seidl, E. Hoffmann, P. Wasserscheid and P. Schühle, A Highly Durable Catalyst System for Hydrogen Production from Dimethyl Ether, *Sustainable Energy Fuels*, 2024, **8**(8), 1740–1749, DOI: [10.1039/d4se00059e](https://doi.org/10.1039/d4se00059e).
 - 27 T. Rüde, S. Dürr, P. Preuster, M. Wolf and P. Wasserscheid, Benzyltoluene/Perhydro Benzyltoluene – Pushing the Performance Limits of Pure Hydrocarbon Liquid Organic Hydrogen Carrier (LOHC) Systems, *Sustainable Energy Fuels*, 2022, **6**(6), 1541–1553, DOI: [10.1039/D1SE01767E](https://doi.org/10.1039/D1SE01767E).
 - 28 C. A. Schneider, W. S. Rasband and K. W. Eliceiri, NIH Image to ImageJ: 25 Years of Image Analysis, *Nat. Methods*, 2012, **9**(7), 671–675, DOI: [10.1038/nmeth.2089](https://doi.org/10.1038/nmeth.2089).
 - 29 G. Bergeret and P. Gallezot, Particle Size and Dispersion Measurements, in *Handbook of Heterogeneous Catalysis*, ed. G. Ertl, H. Knözinger, F. Schüth and J. Weitkamp, Wiley, 2008, pp. 738–765, DOI: [10.1002/9783527610044.hetcacat0038](https://doi.org/10.1002/9783527610044.hetcacat0038).
 - 30 M. Gorgoi, S. Svensson, F. Schäfers, G. Öhrwall, M. Mertin, P. Bressler, O. Karis, H. Siegbahn, A. Sandell, H. Rensmo, W. Doherty, C. Jung, W. Braun and W. Eberhardt, The High Kinetic Energy Photoelectron Spectroscopy Facility at BESSY Progress and First Results, *Nucl. Instrum. Methods Phys. Res., Sect. A*, 2009, **601**(1–2), 48–53, DOI: [10.1016/j.nima.2008.12.244](https://doi.org/10.1016/j.nima.2008.12.244).
 - 31 F. Schaefer, M. Mertin and M. Gorgoi, KMC-1: A High Resolution and High Flux Soft X-Ray Beamline at BESSY, *Rev. Sci. Instrum.*, 2007, **78**(12), 123102, DOI: [10.1063/1.2808334](https://doi.org/10.1063/1.2808334).
 - 32 M. Newville, Larch: An Analysis Package for XAFS and Related Spectroscopies, *J. Phys.: Conf. Ser.*, 2013, **430**, 012007, DOI: [10.1088/1742-6596/430/1/012007](https://doi.org/10.1088/1742-6596/430/1/012007).
 - 33 D. Blaumeiser, R. Stepić, P. Wolf, C. R. Wick, M. Haumann, P. Wasserscheid, D. M. Smith, A.-S. Smith, T. Bauer and J. Libuda, Cu Carbonyls Enhance the Performance of Ru-Based SILP Water–Gas Shift Catalysts: A Combined *in Situ* DRIFTS and DFT Study, *Catal. Sci. Technol.*, 2020, **10**(1), 252–262, DOI: [10.1039/C9CY01852B](https://doi.org/10.1039/C9CY01852B).
 - 34 D. C. Huang, K. H. Chang, W. F. Pong, P. K. Tseng, K. J. Hung and W. F. Huang, Effect of Ag-Promotion on Pd Catalysts by XANES, *Catal. Lett.*, 1998, **53**, 155–159.
 - 35 M. Vanni, M. Serrano-Ruiz, F. Telesio, S. Heun, M. Banchelli, P. Matteini, A. M. Mio, G. Nicotra, C. Spinella, S. Caporali, A. Giaccherini, F. D'Acapito, M. Caporali and M. Peruzzini, Black Phosphorus/Palladium Nanohybrid: Unraveling the Nature of P–Pd Interaction and Application in Selective Hydrogenation, *Chem. Mater.*, 2019, **31**(14), 5075–5080, DOI: [10.1021/acs.chemmater.9b00851](https://doi.org/10.1021/acs.chemmater.9b00851).
 - 36 C. W. Lopes, J. L. Cerrillo, A. E. Palomares, F. Rey and G. Agostini, An *in Situ* XAS Study of the Activation of Precursor-Dependent Pd Nanoparticles, *Phys. Chem. Chem. Phys.*, 2018, **20**(18), 12700–12709, DOI: [10.1039/C8CP00517F](https://doi.org/10.1039/C8CP00517F).
 - 37 E. Sasmaz, C. Wang, M. J. Lance and J. Lauterbach, In Situ Spectroscopic Investigation of a Pd Local Structure over Pd/CeO₂ and Pd/MnO_x–CeO₂ during CO Oxidation, *J. Mater. Chem. A*, 2017, **5**(25), 12998–13008, DOI: [10.1039/C7TA00696A](https://doi.org/10.1039/C7TA00696A).



- 38 A. A. Saraev, S. A. Yashnik, E. Y. Gerasimov, A. M. Kremneva, Z. S. Vinokurov and V. V. Kaichev, Atomic Structure of Pd-, Pt-, and PdPt-Based Catalysts of Total Oxidation of Methane: In Situ EXAFS Study, *Catalysts*, 2021, **11**(12), 1446, DOI: [10.3390/catal11121446](https://doi.org/10.3390/catal11121446).
- 39 M. Takahashi, K. Ohara, K. Yamamoto, T. Uchiyama, H. Tanida, T. Itoh, H. Imai, S. Sugawara, K. Shinohara and Y. Uchimoto, Observation of Subsurface Structure of Pt/C Catalyst Using Pair Distribution Function and Simple Modeling Techniques, *Bull. Chem. Soc. Jpn.*, 2020, **93**(1), 37–42, DOI: [10.1246/bcsj.20190256](https://doi.org/10.1246/bcsj.20190256).
- 40 M. Vaarkamp, F. S. Modica, J. T. Miller and D. C. Koningsberger, Influence of Hydrogen Pretreatment on the Structure of the Metal-Support Interface in Pt/Zeolite Catalysts, *J. Catal.*, 1993, **144**(2), 611–626, DOI: [10.1006/jcat.1993.1357](https://doi.org/10.1006/jcat.1993.1357).
- 41 R. E. Wibowo, R. Garcia-Diez, M. van der Merwe, D. Duarte-Ruiz, Y. Ha, R. Félix, A. Efimenko, T. Bystron, M. Prokop, R. G. Wilks, K. Bouzek, W. Yang, C. Cocchi and M. Bär, Core-Level Spectroscopy with Hard and Soft X-Rays on Phosphorus-Containing Compounds for Energy Conversion and Storage, *J. Phys. Chem. C*, 2023, **127**(42), 20582–20593, DOI: [10.1021/acs.jpcc.3c04704](https://doi.org/10.1021/acs.jpcc.3c04704).
- 42 J. Kruse and P. Leinweber, Phosphorus in Sequentially Extracted Fen Peat Soils: A K-edge X-ray Absorption Near-edge Structure (XANES) Spectroscopy Study, *J. Plant Nutr. Soil Sci.*, 2008, **171**(4), 613–620, DOI: [10.1002/jpln.200700237](https://doi.org/10.1002/jpln.200700237).
- 43 K. D. Szerlag, M. G. Siebecker, F. Izaditame, P. Northrup, R. Tappero and D. L. Sparks, Multimodal, Microspectroscopic Speciation of Legacy Phosphorus in Two US Mid-Atlantic Agricultural Soils, *Soil Sci. Soc. Am. J.*, 2024, **88**(6), 1992–2012, DOI: [10.1002/saj2.20765](https://doi.org/10.1002/saj2.20765).
- 44 S. Beauchemin, D. Hesterberg, J. Chou, M. Beauchemin, R. R. Simard and D. E. Sayers, Speciation of Phosphorus in Phosphorus-Enriched Agricultural Soils Using X-Ray Absorption Near-Edge Structure Spectroscopy and Chemical Fractionation, *J. Environ. Qual.*, 2003, **32**(5), 1809–1819, DOI: [10.2134/jeq2003.1809](https://doi.org/10.2134/jeq2003.1809).
- 45 J. Prietzel, G. Harrington, W. Häusler, K. Heister, F. Werner and W. Klysubun, Reference Spectra of Important Adsorbed Organic and Inorganic Phosphate Binding Forms for Soil P Speciation Using Synchrotron-Based K-Edge XANES Spectroscopy, *J. Synchrotron Radiat.*, 2016, **23**(2), 532–544, DOI: [10.1107/S1600577515023085](https://doi.org/10.1107/S1600577515023085).
- 46 M. Y. Byun, J. S. Kim, D.-W. Park and M. S. Lee, Influence of Synthetic Parameters on the Particle Size and Distribution of Pd in Pd/Al₂O₃ Catalysts, *J. Nanosci. Nanotechnol.*, 2018, **18**(9), 6283–6287, DOI: [10.1166/jnn.2018.15643](https://doi.org/10.1166/jnn.2018.15643).
- 47 H. Dropsch and M. Baerns, CO Adsorption on Supported Pd Catalysts Studied by Adsorption Microcalorimetry and Temperature Programmed Desorption, *Appl. Catal., A*, 1997, **158**(1–2), 163–183, DOI: [10.1016/S0926-860X\(96\)00418-8](https://doi.org/10.1016/S0926-860X(96)00418-8).
- 48 T. Bauer, S. Mehl, O. Brummel, K. Pohako-Esko, P. Wasserscheid and J. Libuda, Ligand Effects at Ionic Liquid-Modified Interfaces: Coadsorption of [C₂C₁Im][OTf] and CO on Pd(111), *J. Phys. Chem. C*, 2016, **120**(8), 4453–4465, DOI: [10.1021/acs.jpcc.6b00351](https://doi.org/10.1021/acs.jpcc.6b00351).
- 49 P. Jakob and A. Schiffer, Coadsorbate Effects on Adsorbate Vibrational Properties, *Surf. Sci.*, 2009, **603**(8), 1135–1144, DOI: [10.1016/j.susc.2009.02.038](https://doi.org/10.1016/j.susc.2009.02.038).
- 50 E. Ozensoy and E. I. Vovk, In-Situ Vibrational Spectroscopic Studies on Model Catalyst Surfaces at Elevated Pressures, *Top. Catal.*, 2013, **56**(15–17), 1569–1592, DOI: [10.1007/s11244-013-0151-x](https://doi.org/10.1007/s11244-013-0151-x).
- 51 P. Hollins, The Influence of Surface Defects on the Infrared Spectra of Adsorbed Species, *Surf. Sci. Rep.*, 1992, **16**(2), 51–94, DOI: [10.1016/0167-5729\(92\)90008-Y](https://doi.org/10.1016/0167-5729(92)90008-Y).
- 52 Y. Sheng, A. Seitz, T. G. Gambu, K. Zhang, P. Schühle and T. Retzer, Site Blocking Effects on P-Modified Pd/Al₂O₃ Catalysts for LOHC Hydrogenation: An in Situ DRIFTS Study, *Catal. Sci. Technol.*, 2025, **15**, 3423–3433, DOI: [10.1039/D4CY01456A](https://doi.org/10.1039/D4CY01456A).
- 53 C. R. Henry, Morphology of Supported Nanoparticles, *Prog. Surf. Sci.*, 2005, **80**(3–4), 92–116, DOI: [10.1016/j.progsurf.2005.09.004](https://doi.org/10.1016/j.progsurf.2005.09.004).
- 54 S. Bertarione, D. Scarano, A. Zecchina, V. Johánek, J. Hoffmann, S. Schauerermann, M. M. Frank, J. Libuda, G. Rupprechter and H.-J. Freund, Surface Reactivity of Pd Nanoparticles Supported on Polycrystalline Substrates As Compared to Thin Film Model Catalysts: Infrared Study of CO Adsorption, *J. Phys. Chem. B*, 2004, **108**(11), 3603–3613, DOI: [10.1021/jp036718t](https://doi.org/10.1021/jp036718t).
- 55 I. V. Yudanov, R. Sahnoun, K. M. Neyman, N. Rösch, J. Hoffmann, S. Schauerermann, V. Johánek, H. Unterhalt, G. Rupprechter, J. Libuda and H.-J. Freund, CO Adsorption on Pd Nanoparticles: Density Functional and Vibrational Spectroscopy Studies, *J. Phys. Chem. B*, 2003, **107**(1), 255–264, DOI: [10.1021/jp022052b](https://doi.org/10.1021/jp022052b).
- 56 M. Kettner, C. Stumm, M. Schwarz, C. Schuschke and J. Libuda, Pd Model Catalysts on Clean and Modified HOPG: Growth, Adsorption Properties, and Stability, *Surf. Sci.*, 2019, **679**, 64–73, DOI: [10.1016/j.susc.2018.08.022](https://doi.org/10.1016/j.susc.2018.08.022).
- 57 A. M. Bradshaw and F. M. Hoffmann, The Chemisorption of Carbon Monoxide on Palladium Single Crystal Surfaces: IR Spectroscopic Evidence for Localised Site Adsorption, *Surf. Sci.*, 1978, **72**(3), 513–535, DOI: [10.1016/0039-6028\(78\)90367-9](https://doi.org/10.1016/0039-6028(78)90367-9).
- 58 A. R. Head, O. Karshoğlu, T. Gerber, Y. Yu, L. Trotochaud, J. Raso, P. Kerger and H. Bluhm, CO Adsorption on Pd(100) Studied by Multimodal Ambient Pressure X-Ray Photoelectron and Infrared Reflection Absorption Spectroscopies, *Surf. Sci.*, 2017, **665**, 51–55, DOI: [10.1016/j.susc.2017.08.009](https://doi.org/10.1016/j.susc.2017.08.009).
- 59 S. Bertarione, Surface Reactivity of Pd Nanoparticles Supported on Polycrystalline Substrates as Compared to Thin Film Model Catalysts: Infrared Study of CH₃OH Adsorption, *J. Catal.*, 2004, **223**(1), 64–73, DOI: [10.1016/j.jcat.2004.01.005](https://doi.org/10.1016/j.jcat.2004.01.005).
- 60 N. M. Martin, M. Van den Bossche, H. Grönbeck, C. Hakanoglu, F. Zhang, T. Li, J. Gustafson, J. F. Weaver and E. Lundgren, CO Adsorption on Clean and Oxidized



- Pd(111), *J. Phys. Chem. C*, 2014, **118**(2), 1118–1128, DOI: [10.1021/jp410895c](https://doi.org/10.1021/jp410895c).
- 61 G. Rupprechter, H. Unterhalt, M. Morkel, P. Galletto, L. Hu and H.-J. Freund, Sum Frequency Generation Vibrational Spectroscopy at Solid–Gas Interfaces: CO Adsorption on Pd Model Catalysts at Ambient Pressure, *Surf. Sci.*, 2002, **502–503**, 109–122, DOI: [10.1016/S0039-6028\(01\)01907-0](https://doi.org/10.1016/S0039-6028(01)01907-0).
- 62 Y. Liu, A. J. McCue, C. Miao, J. Feng, D. Li and J. A. Anderson, Palladium Phosphide Nanoparticles as Highly Selective Catalysts for the Selective Hydrogenation of Acetylene, *J. Catal.*, 2018, **364**, 406–414, DOI: [10.1016/j.jcat.2018.06.001](https://doi.org/10.1016/j.jcat.2018.06.001).
- 63 C. Lu, Q. Zhu, X. Zhang, Q. Liu, J. Nie, F. Feng, Q. Zhang, L. Ma, W. Han and X. Li, Preparation and Catalytic Performance of Metal-Rich Pd Phosphides for the Solvent-Free Selective Hydrogenation of Chloronitrobenzene, *Catalysts*, 2019, **9**(2), 177, DOI: [10.3390/catal9020177](https://doi.org/10.3390/catal9020177).
- 64 J. A. Moulijn, A. E. van Diepen and F. Kapteijn, Catalyst Deactivation: Is It Predictable? What to Do?, *Appl. Catal., A*, 2001, **212**, 3–16.
- 65 R. A. Van Santen, Complementary Structure Sensitive and Insensitive Catalytic Relationships, *Acc. Chem. Res.*, 2009, **42**(1), 57–66, DOI: [10.1021/ar800022m](https://doi.org/10.1021/ar800022m).
- 66 C. Vogt and B. M. Weckhuysen, The Concept of Active Site in Heterogeneous Catalysis, *Nat. Rev. Chem.*, 2022, **6**(2), 89–111, DOI: [10.1038/s41570-021-00340-y](https://doi.org/10.1038/s41570-021-00340-y).
- 67 S. Fuentes and F. Figueras, Hydrogenolysis of Cyclopentane and Hydrogenation of Benzene on Palladium Catalysts of Widely Varying Dispersion, *J. Chem. Soc., Faraday Trans. 1*, 1978, **74**, 174, DOI: [10.1039/f19787400174](https://doi.org/10.1039/f19787400174).
- 68 R. Moss, The Structure and Activity of Supported Metal Catalysts VIII. Chemisorption and Benzene Hydrogenation on Palladium/Silica Catalysts, *J. Catal.*, 1979, **58**(2), 206–219, DOI: [10.1016/0021-9517\(79\)90258-6](https://doi.org/10.1016/0021-9517(79)90258-6).
- 69 S. D. Lin and M. A. Vannice, Hydrogenation of Aromatic Hydrocarbons over Supported Pt Catalysts. I. Benzene Hydrogenation, *J. Catal.*, 1993, **143**(2), 539–553, DOI: [10.1006/jcat.1993.1297](https://doi.org/10.1006/jcat.1993.1297).
- 70 S. D. Lin and M. A. Vannice, Hydrogenation of Aromatic Hydrocarbons over Supported Pt Catalysts. II. Toluene Hydrogenation, *J. Catal.*, 1993, **143**(2), 554–562, DOI: [10.1006/jcat.1993.1298](https://doi.org/10.1006/jcat.1993.1298).
- 71 S. D. Lin and M. A. Vannice, Hydrogenation of Aromatic Hydrocarbons over Supported Pt Catalysts. III. Reaction Models for Metal Surfaces and Acidic Sites on Oxide Supports, *J. Catal.*, 1993, **143**(2), 563–572, DOI: [10.1006/jcat.1993.1299](https://doi.org/10.1006/jcat.1993.1299).
- 72 J. Wang, Q. Li and J. Yao, The Effect of Metal-Acid Balance in Pt-Loading Dealuminated Y Zeolite Catalysts on the Hydrogenation of Benzene, *Appl. Catal., A*, 1999, **184**, 181–188.
- 73 J. Im, H. Shin, H. Jang, H. Kim and M. Choi, Maximizing the Catalytic Function of Hydrogen Spillover in Platinum-Encapsulated Aluminosilicates with Controlled Nanostructures, *Nat. Commun.*, 2014, **5**(1), 3370, DOI: [10.1038/ncomms4370](https://doi.org/10.1038/ncomms4370).
- 74 X. Wang, H. Shi, J. H. Kwak and J. Szanyi, Mechanism of CO₂ Hydrogenation on Pd/Al₂O₃ Catalysts: Kinetics and Transient DRIFTS-MS Studies, *ACS Catal.*, 2015, **5**(11), 6337–6349, DOI: [10.1021/acscatal.5b01464](https://doi.org/10.1021/acscatal.5b01464).
- 75 X. Wang, H. Shi and J. Szanyi, Controlling Selectivities in CO₂ Reduction through Mechanistic Understanding, *Nat. Commun.*, 2017, **8**(1), 513, DOI: [10.1038/s41467-017-00558-9](https://doi.org/10.1038/s41467-017-00558-9).
- 76 C. Chen, J. Lin and H. Chen, Hydrogen Adsorption Sites Studied by Carbon Monoxide Adsorption to Explain the Hydrogenation Activity of Benzene on Pd and Pt Catalysts, *Appl. Catal., A*, 2006, **298**, 161–167, DOI: [10.1016/j.apcata.2005.09.036](https://doi.org/10.1016/j.apcata.2005.09.036).

